Monthly Notices
of the
ROYAL ASTRONOMICAL SOCIETY

MNRAS **483,** 4866–4883 (2019)
Advance Access publication 2018 December 10

doi:10.1093/mnras/sty3351

Dark Energy Survey Year 1 results: measurement of the baryon acoustic oscillation scale in the distribution of galaxies to redshift 1

T. M. C. Abbott,[1] F. B. Abdalla,[2,3] A. Alarcon,[4] S. Allam,[5] F. Andrade-Oliveira,[6,7] J. Annis,[5] S. Avila,[8,9] M. Banerji,[10,11] N. Banik,[5,12,13,14] K. Bechtol,[15] R. A. Bernstein,[16] G. M. Bernstein,[17] E. Bertin,[18,19] D. Brooks,[2] E. Buckley-Geer,[5] D. L. Burke,[20,21] H. Camacho,[6,22] A. Carnero Rosell,[6,23] M. Carrasco Kind,[24,25] J. Carretero,[26] F. J. Castander,[4] R. Cawthon,[27] K. C. Chan,[4,28] M. Crocce,[4] C. E. Cunha,[21] C. B. D'Andrea,[17] L. N. da Costa,[6,23] C. Davis,[21] J. De Vicente,[29] D. L. DePoy,[30] S. Desai,[31] H. T. Diehl,[5] P. Doel,[2] A. Drlica-Wagner,[5] T. F. Eifler,[32,33] J. Elvin-Poole,[34] J. Estrada,[5] A. E. Evrard,[35,36] B. Flaugher,[5] P. Fosalba,[4] J. Frieman,[5,27] J. García-Bellido,[9] E. Gaztanaga,[4] D. W. Gerdes,[35,36] T. Giannantonio,[10,11,37] D. Gruen,[20,21] R. A. Gruendl,[24,25] J. Gschwend,[6,23] G. Gutierrez,[5] W. G. Hartley,[2,38] D. Hollowood,[39] K. Honscheid,[40,41] B. Hoyle,[37,42] B. Jain,[17] D. J. James,[43] T. Jeltema,[39] M. D. Johnson,[24] S. Kent,[5,27] N. Kokron,[6,22] E. Krause,[32,33] K. Kuehn,[44] S. Kuhlmann,[45] N. Kuropatkin,[5] F. Lacasa,[6,46] O. Lahav,[2] M. Lima,[6,22] H. Lin,[5] M. A. G. Maia,[6,23] M. Manera,[2] J. Marriner,[5] J. L. Marshall,[30] P. Martini,[41,47] P. Melchior,[48] F. Menanteau,[24,25] C. J. Miller,[35,36] R. Miquel,[26,49] J. J. Mohr,[42,50,51] E. Neilsen,[5] W. J. Percival,[8] A. A. Plazas,[32] A. Porredon,[4] A. K. Romer,[52] A. Roodman,[20,21] R. Rosenfeld,[6,53] A. J. Ross,[41★] E. Rozo,[54] E. S. Rykoff,[20,21] M. Sako,[17] E. Sanchez,[29] B. Santiago,[6,55] V. Scarpine,[5] R. Schindler,[20] M. Schubnell,[36] S. Serrano,[4] I. Sevilla-Noarbe,[29] E. Sheldon,[56] R. C. Smith,[1] M. Smith,[57] F. Sobreira,[6,58] E. Suchyta,[59] M. E. C. Swanson,[24] G. Tarle,[36] D. Thomas,[8] M. A. Troxel,[40,41] D. L. Tucker,[5] V. Vikram,[45] A. R. Walker,[1] R. H. Wechsler,[20,21,60] J. Weller,[37,42,51] B. Yanny,[5] and Y. Zhang[5] (The Dark Energy Survey Collaboration)

Affiliations are listed at the end of the paper

Accepted 2018 December 4. Received 2018 November 27; in original form 2017 December 18

ABSTRACT

We present angular diameter distance measurements obtained by locating the baryon acoustic oscillations (BAO) scale in the distribution of galaxies selected from the first year of Dark Energy Survey data. We consider a sample of over 1.3 million galaxies distributed over a footprint of 1336 deg^2 with $0.6 < z_{\rm photo} < 1$ and a typical redshift uncertainty of $0.03(1 + z)$. This sample was selected, as fully described in a companion paper, using a colour/magnitude selection that optimizes trade-offs between number density and redshift uncertainty. We investigate the BAO signal in the projected clustering using three conventions, the angular separation, the comoving transverse separation, and spherical harmonics. Further, we compare results obtained from template-based and machine-learning photometric redshift

* E-mail: ashley.jacob.ross@gmail.com

determinations. We use 1800 simulations that approximate our sample in order to produce covariance matrices and allow us to validate our distance scale measurement methodology. We measure the angular diameter distance, D_A, at the effective redshift of our sample divided by the true physical scale of the BAO feature, r_d. We obtain close to a 4 per cent distance measurement of $D_A(z_{eff} = 0.81)/r_d = 10.75 \pm 0.43$. These results are consistent with the flat Λ cold dark matter concordance cosmological model supported by numerous other recent experimental results.

Key words: cosmology: observations – large-scale structure of Universe.

1 INTRODUCTION

The signature of baryon acoustic oscillations (BAO) can be observed in the distribution of tracers of the matter density field and used to measure the expansion history of the Universe. BAO data alone prefer dark energy at greater than 6σ and are consistent with a flat Λ cold dark matter (ΛCDM) cosmology with $\Omega_{matter} = 0.3$ (Ata et al. 2017). A large number of spectroscopic surveys have measured BAO in the distributions of galaxies, quasars, and the Lyman-α forest, including the Sloan Digital Sky Survey (SDSS) I, II, III, and IV (Eisenstein et al. 2005; Gaztañaga, Cabré & Hui 2009; Percival & et al. 2010; Ross et al. 2015a; Alam et al. 2016; Ata & et al. 2017; Delubac et al. 2015; Bautista et al. 2017a), the 2-degree Field Galaxy Redshift Survey (Percival et al. 2001; Cole et al. 2005), WiggleZ (Blake et al. 2011), and the 6-degree Field Galaxy Survey (6dFGS, Beutler et al. 2011).

BAO can also be measured using purely photometric data, though at less significance. Radial distance measurements are severely hampered, but some information about the angular diameter distance D_A is still accessible. Analytic analysis of the expected signal is presented in Seo & Eisenstein (2003), Blake & Bridle (2005), and Zhan, Knox & Tyson (2009). Recently, Ross et al. (2017b, hereafter DES-BAO-$s_\perp$-METHOD) studied the signal expected to be present for data similar to Dark Energy Survey Year 1 (DES Y1) and recommended the use of the projected two-point correlation function, $\xi(s_\perp)$, as a clustering estimator ideal for extracting the BAO signal. Measurements of the BAO signal in various photometric data samples have been presented in Padmanabhan et al. (2007), Estrada, Sefusatti & Frieman (2009), Hütsi (2010), Sánchez et al. (2011), Crocce et al. (2011), Seo et al. (2012), and Carnero et al. (2012), using a variety of methodologies .

We use imaging data from the first year (Y1) of DES observations to measure the angular diameter distance to red galaxies with photometric redshifts $0.6 < z_{photo} < 1.0$. DES is a five-year program to image a 5000 deg^2 footprint of the Southern hemisphere using five passbands, *grizY*. It will measure the properties of over 300 million galaxies. Here, we use 1.3 million galaxies over 1336 deg^2 colour and magnitude selected to balance trade-offs in BAO measurement between the redshift precision and the number density. We use these data, supported by 1800 mock realizations of our sample, to allow us to make the first BAO measurement using galaxies centred at $z > 0.8$.

The measurement we present is supported by a series of companion papers. Crocce et al. (2017) present the selection of our DES Y1 sample, optimized for $z > 0.6$ BAO measurements, tests of its basic properties, and redshift validation; we denote it DES-BAO-SAMPLE hereafter. Avila et al. (2018) describe how 1800 realizations approximating the spatial properties of the DES Y1 data sample were produced and validated; we denote it DES-BAO-MOCKS. Using these mock Y1 realizations, Chan et al. (2018) validate and optimize the methodology for measuring BAO from the angular two-point correlation function, $w(\theta)$; we denote it as DES-BAO-θ-METHOD. Analysis of the angular power spectrum is presented in C_ℓ (Camacho et al. 2018; DES-BAO-ℓ-METHOD).

In this paper, we collate the results of the above papers. With this basic framework, we identify the BAO signature in the DES Y1 data, and use it to place constraints on the comoving angular diameter distance to the effective redshift of our sample, $z_{eff} = 0.81$. The cosmological implications of this measurement are then discussed. Section 2 summarizes the data we use, including all of its basic properties and details on the mock realizations of the data (mocks). Section 3 presents the basic techniques we apply to measure the clustering of galaxies, estimate covariance matrices in order to extract parameter likelihoods, and extract the BAO scale distance from the measurements. Section 4 summarizes tests performed on the 1800 mock Y1 realizations, which help set our fiducial analysis choices. Section 5 presents the clustering measurements and the BAO scale we extract from them. Section 6 compares our measurement to predictions of the flat ΛCDM model and other BAO scale distance measurements. We conclude in Section 7 with a discussion of future prospects.

The fiducial cosmology we use for this work is a flat ΛCDM with $\Omega_{matter} = 0.25$ with $h = 0.7$. Such a low matter density is ruled out by current observational constraints (see e.g. Planck Collaboration et al. 2016). However, the cosmology we use is matched to that of the Marenostrum Institut de Ciències de l'Espai (MICE) (Crocce et al. 2015; Fosalba et al. 2015a,b; Carretero et al. 2015) *N*-body simulation, which was used to calibrate the mock galaxy samples we employ to test and validate our methodology. We will demonstrate that our results are not sensitive to this choice.

We note that the determination of the colour and magnitude cuts, as well as the overall redshift range and the observational systematics treatment, was completed prior to any actual clustering measurement and based on considerations of photo-z performance, area, and number density. Therefore, our sample selection was blind to any potential BAO detection in the data.

2 DATA

2.1 DES Year 1 data

'DES Year 1' (Y1) data were obtained in the period of time between 2013 August 31 and 2014 February 9 using the 570-megapixel Dark Energy Camera (DECam; Flaugher et al. 2015). Y1 contains images occupying a total footprint of more than 1800 deg^2 in *grizY* photometric passbands (Diehl et al. 2014). The DES Data Management (DESDM) system (Mohr et al. 2008; Sevilla et al. 2011; Desai et al. 2012) detrended, calibrated, and co-added these DES images in order to catalogue astrophysical objects. From these results, the Y1 'Gold' catalogue was produced, which provided photometry and 'clean' galaxy samples, as described in Drlica-Wagner et al. (2017). The observed footprint is defined by a HEALPIX (Gorski et al. 2005)

map at resolution $N_{\rm side} = 4096$ and includes only area with a minimum total exposure time of at least 90 s in each of the *griz* bands and a valid calibration solution (see Drlica-Wagner et al. 2017 for details). A series of veto masks, covering regions of poor quality or foregrounds for the galaxy sample, reduce the area to 1336 deg^2 suitable for large-scale structure (LSS) study. We describe the additional masks we apply to the data in Section 2.4.

2.2 BAO sample selection

We use a sample selected from the DES Y1 Gold catalogue to provide the best BAO constraints. The sample balances number density and photometric redshift uncertainty considerations in order to produce an optimal sample. The sample definition is fully described in Crocce et al. (2017, DES-BAO-SAMPLE). We repeat vital information here.

We select our sample based on colour, magnitude, and redshift cuts. The primary redshift, colour, and magnitude cuts are

$$17.5 < i_{\rm auto} < 19.0 + 3.0 z_{\rm BPZ-AUTO} \quad (1)$$

$$(i_{\rm auto} - z_{\rm auto}) + 2.0(r_{\rm auto} - i_{\rm auto}) > 1.7 \quad (2)$$

$$0.6 < z_{\rm photo} < 1.0. \quad (3)$$

The colour and magnitude cuts use `mag_auto` defined in Y1 Gold and $z_{\rm BPZ\text{-}AUTO}$ is the BPZ photometric redshift (Benitez et al. 2000) determined with the `mag_auto` photometry.[1] The quantity $z_{\rm photo}$ is the photometric redshift used for a particular sample, we describe these in Section 2.3.

Stars are removed via the cut

$$\text{spread\_model}_{\rm i} + (5.0/3.0)\text{spreaderr\_model}_{\rm i} > 0.007 \quad (4)$$

and we also remove outliers in colour space via

$$-1 < g_{\rm auto} - r_{\rm auto} < 3 \quad (5)$$

$$-1 < r_{\rm auto} - i_{\rm auto} < 2.5 \quad (6)$$

$$-1 < i_{\rm auto} - z_{\rm auto} < 2. \quad (7)$$

2.3 Redshifts

We define two samples based on two different photometric redshift algorithms, BPZ and DNF (De Vicente, Sánchez & Sevilla-Noarbe 2016). For both samples, our point estimates of the redshift, $z_{\rm photo}$, use photozs determined using the multi-object fit (MOF) photometry defined in Y1 Gold. However, for each sample, we use the BPZ value calculated using `mag_auto` photometry with the sample selection cut defined in equation (1); this is the only time that photozs estimated using `mag_auto` photometry are used. We use the DNF method as our fiducial redshift estimator as it performed better, in terms of both precision and accuracy, on validation tests (see DES-BAO-SAMPLE and DES-BAO-PHOTOZ for more details). As a robustness check, we also compare our results to those derived using BPZ redshifts, as determined using MOF photometry. In Table 1, we present the statistics of each sample (after masking, see Section 2.4) divided into redshift bins of width $\Delta z = 0.1$. We define σ_{68} as the half width of the interval containing the median 68 per cent of values in the distribution of $(z_{\rm photo} - z_{\rm true})/(1 + z_{\rm true})$. This is estimated based on the redshift validation described in DES-BAO-SAMPLE and DES-BAO-PHOTOZ.

[1] While we use `mag_auto` photometry for galaxy selection, our redshift estimates rely on a proper multi-object fitting procedure. The use of `mag_auto` for galaxy selection reflects that the latter colour measurements only became available after the galaxy selection had already been finalized.

Table 1. Characteristics of the DES Y1 BAO sample, as a function of redshift: number of galaxies, redshift uncertainties, and fraction of star contamination. Results are shown for the DNF redshift estimate, with BPZ results in parentheses. We used z to denote the mean redshift of the given estimator (as each galaxy has a redshift likelihood).

$z_{\rm photo}$	$N_{\rm gal}$	$\sigma_{68}/(1+z)$	$f_{\rm star}$
$0.6 < z < 0.7$	386057 (332242)	0.023 (0.027)	0.004 (0.018)
$0.7 < z < 0.8$	353789 (429366)	0.028 (0.031)	0.037 (0.042)
$0.8 < z < 0.9$	330959 (380059)	0.029 (0.034)	0.012 (0.015)
$0.9 < z < 1.0$	229395 (180560)	0.036 (0.039)	0.015 (0.006)

The redshift estimate for each individual galaxy has substantial uncertainty, typically with non-Gaussian likelihood distributions for $z_{\rm true}$. We use individual point estimates of the redshift both for binning in redshift and for calculating transverse separation in h^{-1} Mpc. In order to do so, we use the mean redshift produced by the given redshift estimator. In what follows, we will refer to this estimate of the redshift by z (dropping the photo subscript).

Plots for the estimated true redshift distribution in each of the tomographic bins given in Table 1 are presented in DES-BAO-SAMPLE. For indicative purposes, we quote here estimates of the fraction of galaxies assigned to a redshift bin via their photo-z that would actually lie in a different bin. For the first tomographic bin, 30 per cent for the galaxies are estimated to migrate from the adjacent bins, for the second and third redshift bins this number increases to 40 per cent and for the last bin it is per cent50.

We determine an effective redshift for our sample of $z_{\rm eff} = 0.81$. This is determined from the mean redshift obtained when applying all weights, including those defined in equation (9), which account for the expected signal-to-noise ratio as a function of redshift. See DES-BAO-SAMPLE and DES-BAO-PHOTOZ for further details on the redshifts used for the DES Y1 BAO sample and their validation.

2.4 Mask

The most basic requirement is that DES Y1 observations exist in *griz*, since our selection requires each of the four bands. We use the Y1 Gold coverage maps, at HEALPIX resolution $N_{\rm side} = 4096$, to enforce this condition. We require that any pixel be at least 80 per cent covered in the four bands simultaneously. The minimum coverage across all four bands is then used as a weight for the pixel. We also require that the depth limit in each band is at the level required of our colour/magnitude selection. The Y1 Gold catalogue includes 10σ MAG_AUTO depth maps for each band, again at HEALPIX resolution $N_{\rm side} = 4096$. This is an angular size of 0.014 deg and less than one-tenth of the resolution of any clustering statistics we employ. We consider only areas with *i*-band depth greater than 22 and depth in the other bands great enough to reliably measure the colour defined by equation (2). This involved removing regions of the footprint that did not fulfill the condition $(2r_{\rm maglim} - z_{\rm maglim}) < 23.7$. We further

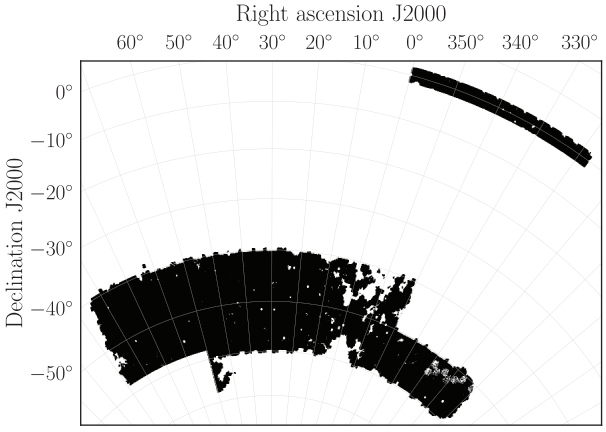

Figure 1. The black shaded region represents the area on the sky to which we restrict our DES Y1 BAO analysis. See Section 2.4.

cut out 'bad regions' identified in Y1GOLD (removing everything with flag bit > 2 in their table 5), and areas with z band seeing greater than 3.7 pixels. We also remove a patch with area 18 deg^2, where the airmass quantity was corrupted. The resulting footprint occupies 1336 deg^2 and is shown in Fig. 1.

2.5 Observational systematics

As detailed in DES-BAO-SAMPLE, we have found significant dependencies between the number density of galaxies in our sample and three observational quantities: the local stellar density, the PSF FWHM ('seeing'), and the detection limit (depth). The dependency with stellar density is understood as stellar contamination: some fraction of our 'galaxies' are in fact stars. The inferred stellar contamination, $f_{\rm star}$, is listed in Table 1. The dependencies with seeing and depth are similar to what was found for a separate DES Y1 sample by Elvin-Poole et al. (2017). We correct for the systematic dependencies via weights that we assign to the catalogue, which when applied remove the trend with the quantity in question. The total weight, $w_{\rm sys}$, is the product of all three individual weights. We apply $w_{\rm sys}$ to all counting and clustering statistics presented in this paper, except where we omit it as a test of robustness. See DES-BAO-SAMPLE for full details on the construction of the weights. We find that the weights have a minimal impact on our analysis.

2.6 Mocks

We simulate our sample using 1800 mock DES Y1 catalogues. These are fully described in Avila et al. (2018, DES-BAO-MOCKS) and we only repeat the basic details here. Each mock matches the footprint, clustering, and redshift accuracy/distribution of our DES sample. Halo catalogues are generated using the HALOGEN technique (Avila et al. 2015), based on a 2LPT density field with an exponential bias. The method is tuned to reproduce the halo clustering as a function of mass and redshift of a reference N-body simulation (MICE; Fosalba et al. 2015a). We use a box size of $L_{\rm box} = 3072\,h^{-1}$ Mpc with a halo mass resolution of $M_{\rm h} = 2.5 \times 10^{12}\,h^{-1}\,{\rm M}_{\odot}$. Haloes are then arranged in a light-cone by superposition of 11 snapshots. We tile eight replicas of the box together using the periodic conditions to construct a full sky mock from $z = 0$ to 1.42, from which we draw eight mock catalogues.

We take care to properly reproduce the redshift properties of our DES Y1 sample. For each mock galaxy, we have the true redshift $z_{\rm true}$. We thus require an estimate of the joint distribution $P(z_{\rm phot}|z_{\rm true})$ in order to assign $z_{\rm phot}$ to each mock galaxy. As detailed in DES-BAO-MOCKS, we find that the sum of a normal and a normal-skewed distribution works well to reproduce our estimates of $P(z_{\rm phot}|z_{\rm true})$ for the DES Y1 data. This method allows us to accurately model the correspondence between the observed redshift $z_{\rm phot}$ and the true redshift $z_{\rm true}$, and its effect on the observed clustering. However, small differences remain between the normalized (to integrate to 1) redshift distribution, $\phi(z)$, for the mocks in each redshift bin and that we estimate for the data. Thus, we will use the $\phi(z)$ specific to the mocks for their BAO template.

Galaxies are added to the mocks using a hybrid Halo Occupation Distribution/Halo Abundance Matching model with three parameters. These are each allowed to evolve with redshift in order to account for bias evolution and selection effects. The amplitude of the clustering in the DES Y1 data is reproduced within approximately 1σ in eight $z_{\rm photo}$ bins with $\Delta z_{\rm photo} = 0.05$ in the range $0.6 < z_{\rm phot} < 1.0$.

Details of the modelling and validation of the mocks can be found in DES-BAO-MOCKS. Here, we use these mock samples to validate our methodology and estimate our covariance matrix, as described in the following section. Other types of mocks have been used in other DES analyses (e.g. MacCrann et al. 2018), however the halogen mocks are the only version of DES mocks that have more than 18 realizations, in fact 1800, while also spanning the full Y1 footprint with sufficient resolution to populate haloes with the typical galaxies of the BAO sample. Having such a large number of mock samples reduces the noise in the derived covariance matrices and is crucial for identifying the proper procedures for dealing with the particularities of the DES Y1 results.

3 ANALYSIS

3.1 Measuring clustering

We perform clustering analysis using both the angular correlation function, $w(\theta)$, and the angular power spectrum measured in spherical harmonics, C_ℓ. We also measure the projected comoving separation correlation function, $\xi(s_\perp, s_{\rm II})$, where $s_\perp$ and $s_{\rm II}$ are the apparent transverse and radial separations. Flat sky approximations are never used for the determination of angular separations.

3.1.1 Angular clustering

In order to calculate $w(\theta)$, we create a uniform random sample within the mask defined in Section 2.2 with size 40 times that of our data sample. We downsample these randoms given the fractional coverage of the pixel (always >0.8 given our mask threshold) to produce the final random sample. Given the random sample, we use the Landy & Szalay (1993) estimator

$$w(\theta) = \frac{{\rm DD}(\theta) - 2{\rm DR}(\theta) + {\rm RR}(\theta)}{{\rm RR}(\theta)}, \quad (8)$$

where, e.g. DD(θ) is the normalized number of pairs of galaxies with angular separation $\theta \pm \Delta\theta$, with $\Delta\theta$ being half the bin size, and all pair counts are normalized based on the total size of each sample. We bin pair counts at a bin size of 0.15 deg, but will combine these to 0.3 deg for our fiducial bin size (as we will find this to be a more optimal data compression in Section 4). We will use both binnings as a test of robustness. We will use $0.5 < \theta < 5$ deg for our fiducial scale cuts, yielding 15θ bins per redshift bin and

thus use 60 total $w(\theta)$ measurement bins. DES-BAO-θ-METHOD demonstrates that adding the results of cross-correlations between redshift bins offers minimal improvement, even when ignoring the degree to which including such measurements would increase the size of the covariance matrix. Thus, we do not consider any such cross-correlations.

The details of the C_ℓ calculation are presented in DES-BAO-ℓ-METHOD. They are measured from the decomposition into spherical harmonics of the projected 2D galaxy overdensity $\delta_{\rm gal}$ in a given redshift bin. To do so, we use the ANAFAST code contained in HEALPIX (Gorski et al. 2005). We then use the pseudo-C_ℓ method given by Hivon et al. (2002) in order to correct for the effect of the masked sky. In our measurements, we use bins of $\Delta\ell = 15$ in the range $30 < \ell < 330$. This $\ell_{\rm max}$ corresponds to a minimum angular scale of $\theta_{\rm min} \approx 0.5^\circ$. We thus use 20 ℓ bins per redshift bin and 80 total C_ℓ measurement bins.

3.1.2 *Projected physical separation correlation function*

We convert our galaxy sample into a 3D map in 'photometric redshift space' by converting angles and redshifts to physical distances. In this way, we are treating the redshift from the photometric redshift estimate like redshifts are used for calculating clustering statistics for a spectroscopic survey. For the corresponding random sample, we use the same angular coordinates of the randoms in the $w(\theta)$ measurements and assign redshifts to the randoms by randomly selecting redshifts from individual galaxies in our galaxy catalogue. We apply a redshift-dependent weight, $w_{\rm FKP}(z)$, based on the number density, galaxy bias (determined by interpolating the results in DES-BAO-MOCKS), and redshift uncertainty as a function of redshift, based on the form derived in DES-BAO-$s_\perp$-METHOD

$$w_{\rm FKP}(z) = \frac{b(z)D(z)}{1 + n_{\rm eff}(z)P_{\rm lin}(k_{\rm eff}, z=0)b^2(z)D^2(z)}, \tag{9}$$

where $n_{\rm eff}(z)$ is the effective number density accounting for the redshift uncertainty (using the equations and methodology described in DES-BAO-$s_\perp$-METHOD), and $k_{\rm eff}$ is the k scale given the greatest weight in Fisher matrix forecasts of the BAO signal, accounting for all of the relevant sample properties.

We calculated normalized pair counts of galaxies and randoms in bins of 1 h^{-1} Mpc along $s_\perp$ and $s_{||}$. Calculating the pair counts with this narrow bin size provides the flexibility to test many different binning schemes. Here, we will combine the pair counts into a bin size of 12 h^{-1} Mpc for our fiducial measurements, but also present tests with many other bin sizes. Additionally, our final results will combine results across shifts in the centre of the bin. This procedure mirrors that used in recent BAO studies (Anderson et al. 2014; Ata et al. 2017). Again, we use a version of the Landy & Szalay (1993) estimator,

$$\xi_{\rm phot}(s_\perp, s_{||}) = \frac{{\rm DD}(s_\perp, s_{||}) - 2{\rm DR}(s_\perp, s_{||}) + {\rm RR}(s_\perp, s_{||})}{{\rm RR}(s_\perp, s_{||})}, \tag{10}$$

where D represents the galaxy sample and R represents the uniform random sample that simulates the selection function of the galaxies. ${\rm DD}(s_\perp, s_{||})$ thus represents the normalized number of pairs of galaxies with separation $s_\perp$ and $s_{||}$. See DES-BAO-$s_\perp$-METHOD for further details. Our fiducial choice employs 14 measurement bins in the range $30 < s_\perp < 200\,h^{-1}$ Mpc. The nature of the measurement means that calculating the clustering over a large redshift window does not dilute the signal like it does for the angular clustering measurements. Therefore, we choose to use the full redshift range when calculating ξ. Thus, the size of the data vector (and thus the covariance matrix) is significantly smaller than that of the angular clustering statistics. The changes in the clustering amplitude and number density as a function of redshift are accounted for by the weights given in equation (9). The mocks mimic these changes and thus any effects are captured in our mock analysis.

The statistic used for ξ measurements is

$$\xi(s_\perp) = \int_0^1 {\rm d}\mu_{\rm obs} W(\mu_{\rm obs}) \xi_{\rm phot}(s_\perp, s_{||}), \tag{11}$$

where the window function $W(\mu_{\rm obs})$ is normalized such that $\int_0^1 {\rm d}\mu_{\rm obs} W(\mu_{\rm obs}) = 1$. $\mu_{\rm obs} = s_{||}/\sqrt{s_\perp^2 + s_{||}^2}$ is the observed cosine of the angle to the line of sight. We have simply used the data with $\mu_{\rm obs} < 0.8$ and adjusted the normalization to compensate, i.e. our $W(\mu)$ is a step function that is 1 for $\mu < 0.8$ and 0 for $\mu > 0.8$. Once more, this matches the approach advocated in DES-BAO-$s_\perp$-METHOD, where it was found that the BAO signal-to-noise ratio and the ability to model it degrades considerably for $\mu > 0.8$.

3.2 Covariance and parameter inference

In order to estimate the covariance matrix for our clustering estimates, we use a large number of mock samples, described in Section 2.6. We have 1800 realizations, so the correlation between data vector, X, elements i and j is

$$C_{\rm i,j} = \frac{1}{1799} \sum_{k=1}^{k=1800} (X_{\rm i}^k - \langle X_{\rm i}\rangle)(X_{\rm j}^k - \langle X_{\rm j}\rangle). \tag{12}$$

For the angular clustering measurements, the full data vector includes multiple redshift bins and the covariance matrix thus includes terms for the covariance of the clustering between different redshift bins.

For angular clustering statistics, we will compare against results obtained from analytic estimates of the covariance matrix. These estimates assume the statistics are that of a Gaussian field. For $w(\theta)$, this is obtained after transforming to configuration space the following expression,

$$\sigma^2(C_\ell) = \frac{2\ell + 1}{f_{\rm sky}(4\pi)^2} (C_\ell + 1/\bar{n})^2 . \tag{13}$$

Full details are given in Section 2.2 of DES-BAO-θ-METHOD, but notably the effect of the survey mask is not included beyond the $f_{\rm sky}$ factor. We denote this as the 'Gaussian' covariance matrix. For C_ℓ, the full details are given in DES-BAO-ℓ-METHOD, but in harmonic space the effect of the shape of the mask is included in the analytic estimate.

The effect of the mask on $w(\theta)$ estimates is studied in DES-BAO-MOCKS. Two different estimates of the $w(\theta)$ covariance matrix determined using mocks are compared to the analytically estimated Gaussian covariance matrix. One matrix is constructed from mocks with the mask for the DES Y1 BAO sample applied and a separate one is constructed by applying a square mask that has the same area. The results are shown in their fig. 12. The diagonal elements of the analytic estimate agree well with the mock estimate using the square mask. The disagreement is worst at small scales for the $0.6 < z < 0.7$ data, which is expected given that this redshift bin has the greatest number density and small scales are expected to have most non-Gaussian influence. When applying the DES Y1 mask to the mocks, significant disagreement is observed at all scales. The mask is also shown to have a significant impact on the off-diagonal component of the covariance matrix. One concludes that the main

need to use the mocks to create the $w(\theta)$ covariance matrix is due to the mask.

DES-BAO-θ-METHOD further investigates the connection between the mock and Gaussian covariance matrices. In one test, they determined that the eigenmodes of the $w(\theta)$ covariance matrix determined using 200 mock realizations can be combined with a Gaussian covariance matrix to produce a covariance matrix matching that produced using the full 1800 mock sample. They also showed that an accurate covariance matrix can be produced via

$$C_{\rm new} = C_{\rm oldMock} - C_{\rm oldGauss} + C_{\rm newGauss}, \quad (14)$$

where 'old' denotes the covariance matrix constructed via mocks assuming some old set of parameters that are used in the construction of the Gaussian covariance matrix and 'new' denotes some new set of parameters we desire to have the covariance matrix for. We will use equation (14) in order to test altering the cosmology assumed when constructing the covariance matrix.

DES-BAO-ℓ-METHOD studied the covariance matrix for the C_ℓ measurements. They applied an analytic method that accounts for the mask, which introduces non-diagonal elements in the covariance, as well as the number density and the level of clustering. At high ℓ, it was observed that the mock C_ℓ have lower amplitude than observed for the DES data. The analytic covariance matrix was thus constructed using analytic C_ℓ matching the observed level of clustering at all scales. This analytic covariance produced a moderate improvement in the recovered χ^2/dof for the best-fitting model (85.8/63 compared to 93.7/63). We note that, in contrast to the C_ℓ results, the mocks are in excellent agreement with the configuration space measurements obtained from the data and we therefore trust the use of mock covariance matrix for such statistics.

The cosmology used to produce the mocks is significantly different from that preferred by current data. The difference in the expected BAO scale when comparing our fiducial cosmology and that preferred by Planck Collaboration et al. (2016) is 4 per cent, which is a close match to our expected precision. The agreement presented in DES-BAO-MOCKS demonstrates that the clustering of the DES Y1 BAO sample would be unlikely to rule out our fiducial cosmology. Previous studies (e.g. Labatie, Starck & Lachièze-Rey 2012; Taylor, Joachimi & Kitching 2013; Morrison & Schneider 2013; White & Padmanabhan 2015) on the cosmological dependence of the covariance matrix generally conclude one should be most worried when the data being tested would reject the cosmology assumed to construct the covariance matrix. We test for any impact on our results due to the assumed cosmology explicitly, using equation (14) to produce a covariance matrix at the Planck Collaboration et al. (2016) cosmology, in Section 5.

The impact of choices used in the construction of covariance matrices used for SDSS-III galaxy BAO measurements was studied as part of Vargas-Magaña et al. (2018). Two sets of mocks were used, using separate approximate methods, as was an analytic approach. They found no significant expected shift in the BAO measurement when using the covariance matrix from one method to measure the BAO on either set of mocks. However, Vargas-Magaña et al. (2018) did find 10 per cent level variation in the recovered size of the uncertainty depending on the covariance matrix that was used. We therefore expect a similar level of uncertainty on our uncertainty determination. We use the covariance matrix determined from our 1800 mock realizations, given by equation (12), throughout unless otherwise noted.

When using mocks to estimate covariance matrices, we must account for the noise imparted due to the fact we use a finite set of realizations. This noise introduces biases into the inverse covariance matrix. Thus, corrections must be applied to the χ^2 values, the width of the likelihood distribution, and the standard deviation of any parameter determined from the same set of mocks used to define the covariance matrix. These factors are defined in Hartlap, Simon & Schneider (2007), Dodelson & Schneider (2013), and Percival et al. (2014). Given that we use 1800 mocks, these factors are at most 3.6 per cent.

We use the standard χ^2 analysis to quantify the level of agreement between data and model vectors and to determine the likelihood of parameter values. Given a covariance matrix, C, representing covariance of the elements of a data vector, and the difference D between a data vector and model data vector, the χ^2 is given by

$$\chi^2 = D\mathsf{C}^{-1}D^T. \quad (15)$$

The likelihood, $\mathcal{L}$, of a given parameter, p, is then

$$\mathcal{L}(p) \propto {\rm e}^{-\chi^2(p)/2}. \quad (16)$$

3.3 Determining the BAO scale

In order to extract the BAO scale from each clustering statistic, we use a template-based method. This approach was used in Seo et al. (2012), Xu et al. (2012), Anderson et al. (2014), and Ross et al. (2017a). The template is derived from a linear power spectrum, $P_{\rm lin}(k)$, with 'damped' BAO modelled using a parameter $\Sigma_{\rm nl}$ (defined below) that accounts for the smearing of the BAO feature due to non-linear structure growth. We first obtain $P_{\rm lin}(k)$ from CAMB[2] (Lewis, Challinor & Lasenby 2000) and fit for the smooth 'no-wiggle'[3] $P_{\rm nw}(k)$ via the Eisenstein & Hu (1998) fitting formulae with a running spectral index. We account for redshift-space distortions (RSD) and non-linear effects via

$$P(k,\mu) = (1+\mu^2\beta)^2\left((P_{\rm lin}-P_{\rm nw}){\rm e}^{-k^2\Sigma_{\rm nl}^2}+P_{\rm nw}\right), \quad (17)$$

where $\mu = \cos(\theta_{\rm LOS}) = k_{||}/k$, and $\beta \equiv f/b$. This factor is set based on the galaxy bias, b, and effective redshift of the sample we are modelling, with f defined as the logarithmic derivative of the growth factor with respect to the scale factor. The factor $(1+\beta\mu^2)^2$ is the 'Kaiser boost' (Kaiser 1987), which accounts for linear-theory RSD. The BAO 'damping' factor is

$$\Sigma_{\rm nl}^2 = (1-\mu^2)\Sigma_\perp^2/2 + \mu^2\Sigma_{||}^2/2. \quad (18)$$

Given that we have little sensitivity to the line of sight, we will only test varying $\Sigma_{\rm nl}$ (as opposed to its transverse and line-of-sight components separately), i.e. we use a μ independent $\Sigma_{\rm nl}$ in equation (17).

Each of $\xi(s_\perp)$, $w(\theta)$, and C_ℓ require one or both of the combination of Fourier transforming and projecting equation (17) over redshift distributions or uncertainties, in order to obtain the BAO template, $T_{\rm BAO}(x)$, as a function of scale, x.[4] For both of the configuration space templates, the anisotropic redshift-space correlation function, $\xi_s(s,\mu)$ is obtained from the Fourier transform of $P(k,\mu)$ defined above. For the angular statistics, we project over the redshift distribution, $\phi(z)$, normalized to integrate to 1. For $w(\theta)$, we have

$$w(\theta) = \int {\rm d}z_1 \int {\rm d}z_2 \phi(z_1)\phi(z_2)\xi_s(s[z_1,z_2,\theta],\mu[z_1,z_2,\theta]). \quad (19)$$

[2] camb.info

[3] Models using only this component will be labelled 'noBAO' in plots.

[4] Here, x represents either $r_\perp$, θ, or ℓ depending on the statistic in question.

Further details can be found in DES-BAO-θ-METHOD. For harmonic space, we have

$$C_\ell = \frac{2}{\pi}\int \mathrm{d}k k^2 P(k, \mu = 0)\Psi_\ell^2, \tag{20}$$

with

$$\Psi_\ell = \phi(x) j_\ell[k\chi(z)], \tag{21}$$

where $\chi(z)$ is the comoving distance to z and Ψ_ℓ is modified to account for RSD as described in DES-BAO-ℓ-METHOD.

When modelling the projected correlation function $\xi(s_\perp)$, we follow the formalism of Ross et al. (2017b), which strictly speaking is only appropriate for Gaussian photometric redshift errors. Our model for $\xi(s_\perp)$ is as follows

$$\xi(s_\perp, \mu) = \int \mathrm{d}z G(z)\xi(s_{\rm true}[s_\perp, \mu, z], \mu_{\rm true}[s_\perp, \mu, z]), \tag{22}$$

where $G(z)$ is a normal distribution of width $\sqrt{2}\sigma_z$ and we used the weighted average of the σ_{68} quantities listed in Table 1. The $s_\perp$ and μ quantities are those we observe in DES, in the presence of redshift uncertainties, thus requiring the distinction between them and the 'true' quantities involved in the projection. See DES-BAO-$s_\perp$-METHOD for more details.

Note that unlike our treatment of $\xi(s_\perp)$, our treatment of the angular correlation function does not assume that the photometric redshift are Gaussian, and is in fact completely general. This is a primary reason that we adopt our measurement of the angular correlation function as our fiducial analysis. We still explore whether an analysis of the projected correlation function produces consistent results, while possibly reducing the statistical error budget. The impact of the Gaussian photo-z assumption for $\xi(s_\perp)$ is further discussed in the following sections.

For each statistic, the BAO scale is obtained through

$$M(x) = BT_{\rm BAO}(x\alpha') + A(x), \tag{23}$$

where the parameter α' rescales the separation to allow a match between the BAO feature in the theory and observation. In configuration space, it is simply α [so e.g. $x\alpha' = \theta\alpha$ for $w(\theta)$], but in harmonic space $\alpha' = 1/\alpha$ (so $x\alpha' = \ell/\alpha$). Therefore, α parametrizes the BAO measurement (how different the BAO position is in the measurement versus assumed by the template). The parameter B allows the amplitude to change (e.g. due to galaxy bias), and $A(x)$ is a free polynomial meant to account for any differences in between the broad-band shape in the data and template. These differences can be due to, e.g. differences between the fiducial and true cosmology and observational systematic effects. Therefore, including the polynomial helps both to isolate BAO scale information and make the measurements robust. Generally, a three-term polynomial is used, e.g. for $\xi(s_\perp)$, $A(s_\perp) = a_1 + a_2/s_\perp + a_3/s_\perp^2$. Similar expressions hold for $A(\theta)$ and $A(\ell)$. Details can be found in DES-BAO-θ-METHOD and DES-BAO-ℓ-METHOD.

For $w(\theta)$ we determine $\Sigma_{\rm nl}$ by fitting to the mean $w(\theta)$ of the mocks. We have fitted to each redshift bin individually. We find that a constant damping scale of 5.2 h^{-1} Mpc offers a good fit to all four redshift bins. Based on the modelling described in DES-BAO-θ-METHOD, we expect to find a value consistent with the transverse damping scale for spectroscopic redshift space. Indeed, our recovered value is close to the value of 5.6 h^{-1} Mpc one obtains when extrapolating the discussion preceding equation (3) of Seo & Eisenstein (2007) to $z = 0.8$ and $\sigma_8 = 0.8$. See DES-BAO-θ-METHOD for more details. Thus, we will use this damping scale when fitting to the $w(\theta)$ mocks and data, though we will demonstrate our results are robust against this choice.

We repeat the procedure in order to find a best-fitting $\Sigma_{\rm nl}$ for $\xi(s_\perp)$. In principle, we should find the same result as found for $w(\theta)$. However, our modelling DES-BAO-$s_\perp$-METHOD assumes Gaussian redshift uncertainties, while the true distributions have significant non-Gaussian tails DES-BAO-MOCKS. Given that the size of the BAO feature depends strongly on the redshift uncertainty, we might expect that our inaccuracies in the treatment of the redshift uncertainty translates to finding a best-fitting $\Sigma_{\rm nl}$ that is greater than the theoretical expectation. Indeed, we find $\Sigma_{\rm nl} = 8\,h^{-1}$ Mpc; just over 50 per cent larger than both the value found for $w(\theta)$ and the theoretical expectation. We thus set $\Sigma_{\rm nl} = 8\,h^{-1}$ Mpc for our fiducial $\xi(s_\perp)$ model, to also account for the known inaccuracies with respect to modelling the redshift uncertainties. We will explore the sensitivity of the results obtained from the DES Y1 mocks and the data to this choice. We will improve the modelling in future analyses.

Each method allows us to obtain the likelihood $L(\alpha)$, which represents our BAO measurement. This can be converted to a likelihood for the angular diameter distance $D_{\rm A}$ at the effective redshift of our sample, $z_{\rm eff}$, via

$$\alpha = \frac{D_{\rm A}(z_{\rm eff})r_{\rm d}^{\rm fid}}{D_{\rm A}^{\rm fid}(z_{\rm eff})r_{\rm d}}, \tag{24}$$

where $r_{\rm d}$ is the sound horizon at the drag epoch (and thus represents the expected location of the BAO feature in comoving distance units, due to the physics of the early Universe). The superscript $^{\rm fid}$ denotes that the fiducial cosmology was used to determine the value. In this work, $r_{\rm d}^{\rm fid} = 153.44$ Mpc. One can see that equation (24) can be re-arranged to obtain

$$\frac{D_{\rm A}(z_{\rm eff})}{r_{\rm d}} = \alpha\frac{D_{\rm A}^{\rm fid}(z_{\rm eff})}{r_{\rm d}^{\rm fid}}. \tag{25}$$

The likelihood we obtain for $\alpha\frac{D_{\rm A}(z_{\rm eff})}{r_{\rm d}}$ can directly be used to constrain cosmological models. In a flat geometry, $D_{\rm A}$ is given by

$$D_{\rm A}(z) = \frac{c}{H_0(1+z)}\int_0^z \mathrm{d}z'\frac{H_0}{H(z')}. \tag{26}$$

In our fiducial cosmology, $D_{\rm A}(0.81) = 1597.2$ Mpc. The fiducial $D_{\rm A}(0.81)/r_{\rm d}$ is thus 10.41.

Notably, we are making an implicit assumption that the relative dependence of $D_{\rm A}$ on cosmological parameters is constant over the redshift range of our sample ($0.6 < z < 1.0$), as even for the statistics where we bin in redshift ($w(\theta)$ and C_ℓ) we are determining a single α likelihood. This is not a perfect assumption, as, e.g. the relative shift in $D_{\rm A}$ between our fiducial cosmology and the Planck Collaboration et al. (2016) cosmology between $z = 0.6$ and 1.0 is one per cent. This can be compared to the total shift at the effective redshift $z = 0.81$ of 4.2 per cent. In effect, our use of the single α means we are not optimally analysing the signal. Zhu, Padmanabhan & White (2015) present methodology for a more optimal redshift-space analysis, though Zhu et al. (2018) do not find major improvements over the type of analysis we present when applying the methodology to a quasar sample occupying $0.8 < z < 2.2$. Finally, we note that Bautista et al. (2018) use the same redshift range for BAO measurements as we do in this analysis.

Our DES Y1 sample is in a regime with an expected signal-to-noise ratio, in terms of detection ability, of close to 2. In such a regime, we do not expect Gaussian likelihoods. In general for low signal-to-noise BAO measurements, the tails of the distribution extend to both large and small values of α. See e.g. Ross et al. (2015a)

and Ata et al. (2017) for recent similar signal-to-noise BAO measurement and DES-BAO-θ-METHOD for a detailed investigation of what we expect for DES Y1 $w(\theta)$ measurements. Indeed, we find such tails in our DES Y1 analysis and one consequence is that when using our 1800 mock catalogues, we find that 8 per cent of the realizations lead to no clear detection of the BAO feature. An important consequence of these facts is that it is critically important for any cosmological application of our results to consider the full likelihood. We restrict our analysis to $0.8 < \alpha < 1.2$, equivalent to obtaining the posterior likelihood assuming a flat prior on α in this range. This posterior likelihood will be released as a $\chi^2(\alpha)$ lookup table after this work has been accepted for publication.

In the interest of reporting a meaningful summary statistic, we restricted ourselves to the fraction of mock realizations in which the BAO feature was detected (92 per cent), and calculated the error in α by demanding $\Delta\chi^2 = 1$ relative to the maximum likelihood point. This is the error that we report throughout. Our approach matches that of Ross et al. (2015a) and Ata et al. (2017), who faced similar issues. When restricting ourselves to mock galaxy catalogues with a BAO detection, we found that this error corresponds to a 68 per cent confidence region for $w(\theta)$ (see DES-BAO-θ-METHOD for details, where alternative approaches are also explored and where the approach we adopt is determined to be the best option) and we apply the same criteria to each clustering statistic we use, as each is fit using the same basic methodology. Thus, while this quantity is not formally a 68 per cent confidence region for our posterior likelihood, we have opted for utilizing this quantity as a summary statistic. In practice, all cosmological inferences from our results will utilize our full posterior likelihood.

4 TESTS ON MOCKS

In this section, we report the results of testing our BAO fitting methodology on the 1800 mock realizations. We test fits to both the mean of these mocks and each mock individually. These tests inform how we obtain our final consensus Y1 BAO measurement and how we decide fiducial settings such as bin size and the range of scales considered. We report the results of tests for each clustering statistic we present BAO measurements for. Additional tests for $\xi(s_\perp)$ and $w(\theta)$ measurements can be found in DES-BAO-$s_\perp$-METHOD and DES-BAO-θ-METHOD, with implications beyond the DES Y1 sample. The motivation for fiducial choices for the $w(\theta)$ analysis are described in DES-BAO-θ-METHOD. We divide the section into tests done on the mean of the mocks (giving us one data vector with the signal to noise for 1800 DES Y1) and tests done on each individual mock (providing distributions for the signal to noise we should expect to recover).

4.1 Test on mean statistics

The total number of mock realizations has high signal-to-noise ratio. In principle, we should divide our covariance matrix by 1800 in order to fit the mean of the mocks. However, we are primarily interested in the uncertainty we should expect for DES Y1, and thus we will quote results obtained either from the nominal covariance matrix for DES Y1 or with the appropriate scaling.

First, we determine the fiducial bin size for the $\xi(s_\perp)$ analysis by fitting to the mean $\xi(s_\perp)$ of the 1800 mock realizations. If not for noise from the covariance matrix, using the smallest bin size possible would always maximize the signal-to-noise ratio. However, the noise in the covariance matrix increases with its number of elements and thus the optimal bin size will be somewhat greater than the size where significant information starts to be lost. The signal-to-noise ratio for one realization is such that the likelihoods are typically non-Gaussian. As the signal-to-noise ratio of BAO measurements increases, the likelihoods typically become well approximated by Gaussians (e.g. compare Ross et al. 2015a to Anderson et al. 2014). To take advantage of this, we divide the DES Y1 covariance matrix obtained from the mocks by 10 and obtain the likelihood. We then obtain α and σ as usual but define a 'Gaussian' uncertainty $\sigma_G = \sqrt{10}\sigma$. The results are unchanged if we use a factor of 20 rather than our factor of 10. The results are presented in Table 2. We find that the optimal results are expected for a bin size of $12\,h^{-1}$ Mpc. This is significantly greater than the optimal bin size typically found for spectroscopic surveys; a potential explanation is that the redshift uncertainty has significantly smeared the BAO, making a narrow bin size less important for recovering the total signal (see fig. 1 of Ross et al. 2017b).

Table 2. The expected uncertainty for DES Y1 data, assuming a Gaussian likelihood applied to the mean $\xi(s_\perp)$ obtained from 1800 mock realizations, as a function of the $s_\perp$ binning that is used. See the text for details.

Binning	σ_G
$0.6 < z < 1.0$:	
$\Delta s_\perp = 5\,h^{-1}$ Mpc	0.054
$\Delta s_\perp = 8\,h^{-1}$ Mpc	0.053
$\Delta s_\perp = 10\,h^{-1}$ Mpc	0.052
$\Delta s_\perp = 12\,h^{-1}$ Mpc	0.051
$\Delta s_\perp = 15\,h^{-1}$ Mpc	0.052
$\Delta s_\perp = 20\,h^{-1}$ Mpc	0.059

Table 3. BAO fits to the mean Y1 mocks. The α values suggest how biased our fitting methods are and the σ represents something akin to a Fisher matrix prediction for the precision we should achieve on the data. The fiducial analysis choices for $\xi(s_\perp$ are $30 \le s_\perp < 200\,h^{-1}$ Mpc and $\Delta s_\perp = 12\,h^{-1}$ Mpc. For $w(\theta)$, they are $0.5 < \theta < 5$ deg and $\Delta\theta = 0.3$ deg.

Case	α
$0.6 < z < 1.0$:	
$w(\theta)$	1.003 ± 0.055
$w(\theta)$, $\theta_{\rm min} = 1$ deg	1.003 ± 0.055
$w(\theta)$, $\Delta\theta = 0.15$ deg	1.004 ± 0.057
C_ℓ	1.009 ± 0.056
ξ	1.007 ± 0.052
ξ, $s_{\perp,\rm min} = 50\,h^{-1}$ Mpc	1.008 ± 0.052
ξ, $\Sigma_{\rm nl} = 4\,h^{-1}$ Mpc	1.005 ± 0.045
ξ, $\Sigma_{\rm nl} = 12\,h^{-1}$ Mpc	1.009 ± 0.065

Table 3 displays results for fits to the mean of the 1800 mocks, using the DES Y1 covariance matrix. For our fiducial analysis choices, we expect an uncertainty of just greater than 5 per cent. We also see that choosing $s_{\perp,\rm min} = 30\,h^{-1}$ Mpc opposed to $50\,h^{-1}$ Mpc improves the results both in terms of the bias in α and the recovered uncertainty. For $w(\theta)$, using a larger bin size of 0.3 deg improves the results compared to 0.15 deg. This is due to the fact that the number of elements in the covariance matrix is reduced from 120^2 to 60^2, significantly reducing the required correction factors. DES-BAO-θ-METHOD reports further tests of the bin size, suggesting no significant improvement is to be achieved compared to the fiducial 0.3 deg bin size. We further see that we expect to recover slightly smaller uncertainties from ξ compared to $w(\theta)$ or C_ℓ, but this is at most a 5 per cent difference. Further tests of the C_ℓ are detailed in Camacho et al. (2018).

Table 4. Statistics for BAO fits on mocks. $\langle\alpha\rangle$ is either the BAO dilation scale measured from the correlation function averaged over all of the mocks (denoted 'mean'), or the mean of the set of dilation scales recovered from mocks with $>1\sigma$ BAO detections. $\langle\sigma\rangle$ is the same for the uncertainty obtained from $\Delta\chi^2 = 1$ region. S is the standard deviation of the α recovered from the mock realizations with $>1\sigma$ BAO detections and $f(N_{\rm det})$ is the fraction of realizations satisfying the given condition.

Case	$\langle\alpha\rangle$	$\langle\sigma\rangle$	S_α	$f(N_{\rm det})$
$0.6 < z < 1.0$:				
$\xi + w$	1.004	0.050	0.050	0.917
$w + C_\ell$	1.006	0.055	0.052	0.901
$w(\theta)$	1.001	0.051	0.054	0.898
$w(\theta)$, $\Delta\theta = 0.15$ deg	1.001	0.054	0.055	0.907
$w(\theta)$, $\theta_{\rm min} = 1$ deg	1.002	0.051	0.053	0.898
C_ℓ	1.007	0.058	0.053	0.864
ξ (bins combined)	1.004	0.048	0.050	0.916
ξ, $+0\,h^{-1}$ Mpc	1.004	0.048	0.050	0.916
ξ, $+3\,h^{-1}$ Mpc	1.004	0.048	0.051	0.916
ξ, $+6\,h^{-1}$ Mpc	1.005	0.048	0.050	0.916
ξ, $+9\,h^{-1}$ Mpc	1.005	0.048	0.050	0.921
ξ, $s_{\perp{\rm min}} = 50\,h^{-1}$ Mpc	1.005	0.049	0.050	0.913
ξ, $\Delta s_\perp = 5\,h^{-1}$ Mpc	1.005	0.050	0.051	0.918
ξ, $\Delta s_\perp = 10\,h^{-1}$ Mpc	1.005	0.049	0.050	0.916
ξ, $\Delta s_\perp = 15\,h^{-1}$ Mpc	1.004	0.048	0.051	0.911

The α obtained from the mean of the mocks is biased high for all three methods we have tested. For the uncertainty expected from a single Y1 realization, it is a 0.06σ (0.003) bias for $w(\theta)$, 0.13σ (0.007) for ξ, and 0.16σ (0.009) for C_ℓ. This is small enough to not be a significant concern for the Y1 signal-to-noise ratio. However, given that this is the mean of 1800 mocks, the significance of the detection of a bias is 6.8σ for C_ℓ, 5.6σ for ξ, and only 2.3σ for $w(\theta)$. This suggests that it is a true bias that will need to be addressed as the signal-to-noise ratio increases for future data samples. We will use the $w(\theta)$ results for our DES Y1 measurement, where the bias is only of marginal significance. As detailed in, e.g. both Crocce & Scoccimarro (2008) and Padmanabhan & White (2009), a small positive bias is expected from non-linear structure growth, which could explain ∼0.003 worth of the bias and thus fully account for the $w(\theta)$ results.

4.2 Tests on individual mocks

Results obtained from fitting each individual mock realization are shown in Table 4. We denote the mean and standard deviation of any measured quantity x across realizations using $\langle x\rangle$ and S_x. Results are shown for cases where there is a $\Delta\chi^2 = 1$ region within $0.8 < \alpha < 1.2$; these are referred to as 'detections' (and those mocks where this is not the case are 'non-detections'). For $\xi(s_\perp)$ just over 91 per cent of the mocks yield a detection, while for $w(\theta)$ it is just less than 90 per cent. The results are generally consistent with the tests on the mean of the mocks. We learn that the standard deviation and mean uncertainties are matched to within 4 per cent. The mean uncertainties are generally slightly smaller than the standard deviations, reflecting the fact that the likelihoods have non-Gaussian tails and we are using $\Delta\chi^2 = 1$ to quote the uncertainty.

For all three methods, the biases in α have decreased slightly, though this is likely due to our detection criteria within $0.8 < \alpha < 1.2$ (since it is symmetric around $\alpha = 1$ instead of $\alpha \sim 1.005$). The uncertainties for $w(\theta)$ are only 5 per cent greater than for ξ, and the C_ℓ results are somewhat less precise than the $w(\theta)$ results. In

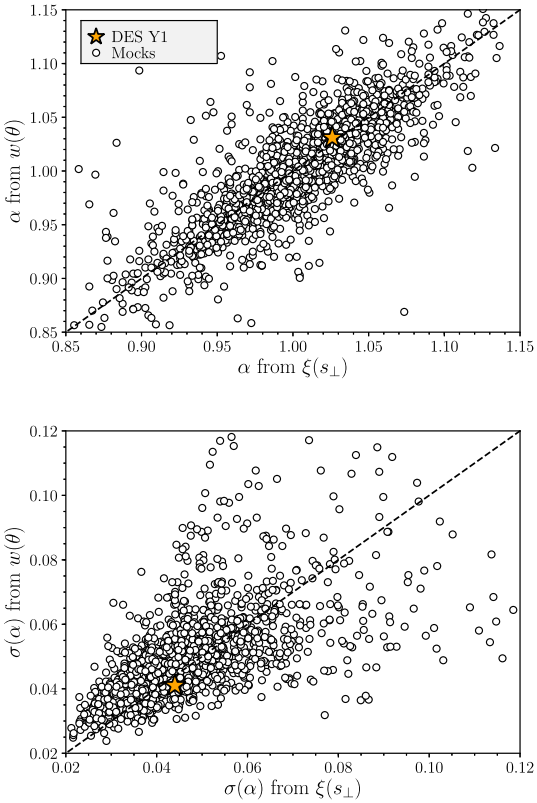

Figure 2. A comparison of $w(\theta)$ and $\xi(s_\perp)$ BAO fit parameter α and its uncertainty performed on mock realizations (white circles) and the DESY1 data (stars). The mock realizations are for $0.6 < z < 1.0$. The uncertainty, σ, is obtained from the $\Delta\chi^2 = 1$ definition (see the text).

configuration space, varying the bin size or minimum scale does not reveal any large changes in the results. Further tests are performed on the C_ℓ measurements in DES-BAO-ℓ-METHOD. In particular, the mocks are used to determine the optimal range in ℓ, the bin size in ℓ, and the number and type of polynomial broad-band terms to use. The results presented here show their optimized choices.

For $\xi(s_\perp)$, we also vary the centre of the bin, in steps of $3\,h^{-1}$ Mpc, and combine the results by taking the mean of the resulting four likelihoods. This process is similar to that of Ross et al. (2015a) and Ata et al. (2017), where it was found such a procedure provides small improvements in the accuracy of both the recovered α and its uncertainty. We find that this process has a small effect on the results. The standard deviation is not improved at the level reported in Table 4, but comparing the combined result to the $+0\,h^{-1}$ Mpc result, there is a one per cent improvement in the standard deviation for the combined results. The biggest change from combining the likelihoods is that there is somewhat less dispersion in the uncertainty recovered from the likelihood. In the $+0\,h^{-1}$ Mpc case, the standard deviation of the uncertainties is 0.018, while after combining it is reduced to 0.017. We also determine the standard deviation of the scatter, per mock, for the results in each of the four bin centres. We find 0.004 (so this is the level of difference we expect to find when repeating these tests on the DES Y1 data).

Fig. 2 compares the results of BAO fits to the mocks for ξ and $w(\theta)$ using white circles. The results are shown only for realizations that have detection for both statistics, which is 1565 realizations (87 per cent). Stars represent the results for the DES Y1 data and are discussed in Section 5. The bottom panel displays the results for

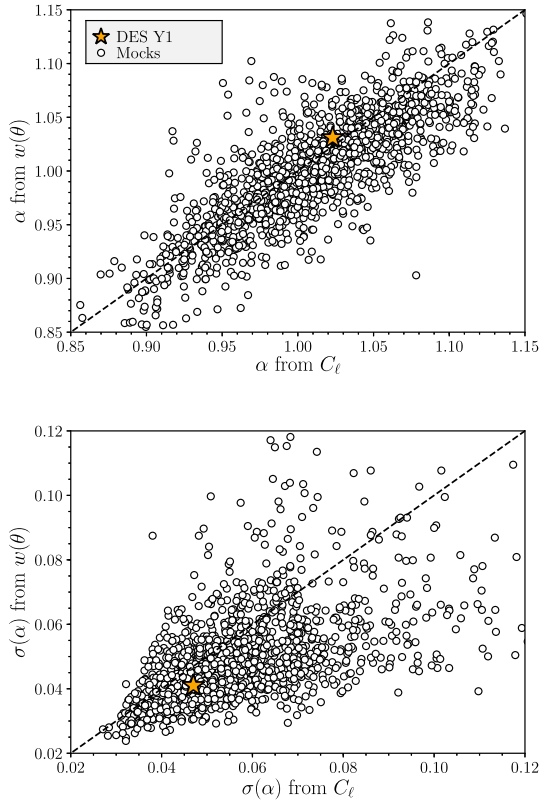

Figure 3. Same as Fig. 2, but the C_ℓ results replace $\xi(s_\perp)$.

the value of α. As expected, the two results are correlated, though there is significant scatter. The correlation factor is 0.81, while for these realizations the standard deviation in the ξ results is 0.048 and it is 0.051 for $w(\theta)$. Taking their mean, the standard deviation is reduced to 0.047; this suggests some small gain is possible from combining the measurements. The top panel displays the results for the recovered uncertainty. ξ recovers a lower uncertainty on average, but there is a large amount of scatter. We test our results when taking the mean of the $\xi(s_\perp)$ and $w(\theta)$ likelihoods, labelled '$\xi + w$' in Table 4. We find mean uncertainty matching the standard deviation at 0.050 and the highest fraction of 'detections'. However, the gain in the precision from the combination is similar to the shift in α (away from the unbiased value of 1), suggesting the gain from combining the results is not worthwhile for the cases where $w(\theta)$ has sufficient signal-to-noise ratio on its own for a robust measurement.

Fig. 3 repeats the comparison, but substitutes the C_ℓ results for ξ. 1502 (83 per cent of) mock realizations have a $\Delta\chi^2 = 1$ bound within $0.8 < z < 1.2$ for both statistics. As expected, the results are strongly correlated in α, with a correlation factor of 0.80. The orange star represents the α values recovered for the DES Y1 data; the fact that it lies within the locus of points representing the mock realizations suggests the differences we found in α are typical. The same is true for the recovered uncertainty, where there is a fairly large dispersion but the uncertainty recovered from the C_ℓ measurements is greater on average. Correspondingly, for this selection of mock realizations the standard deviation in α is slightly greater for the C_ℓ: 0.052 compared to 0.051. Like for the $\xi + w$ results, we obtain results by using the mean of the C_ℓ and $w(\theta)$ likelihoods. Similar to the $\xi + w$ case, the number of detections and the standard deviation are improved over the case of using either statistic alone, but the $\langle\alpha\rangle$ has shifted away from 1 to become more biased and this shift greater than the gain in precision. The result once more suggests that combining the results is unlikely to worthwhile for the DES Y1 data.

The strength of the BAO feature, and thus its signal-to-noise ratio, in any particular realization of the data can vary. This is clear from the wide range of uncertainties shown in Fig. 2, and is consistent with previous BAO analyses (see e.g. fig. 10 of Ata et al. 2017). We can use the mocks to determine the extent to which the scatter in the uncertainties recovered from the likelihood are truly representative of the variance in the ability to estimate the BAO parameter α. We do so by dividing the mock samples into bins based on the recovered uncertainty and comparing to the standard deviation of α values in each bin, using the mean of the $\xi + w$ likelihoods. Dividing into bins with approximately the same number of mocks in each (to within 30 mocks), the mean uncertainty and standard deviations are $\langle\sigma\rangle, S_\alpha = (0.035, 0.039), (0.043, 0.049), (0.052, 0.054)$, and (0.073, 0.055). For the mock realizations with the highest uncertainty, the scatter in α values is significantly smaller. This is likely due to the fact that the α values must lie within $(0.8 + \sigma, 1.2 - \sigma)$ in order to be counted as a detection and this therefore decreases their standard deviation. At lower values of uncertainty, there is a clear correlation between the mean recovered uncertainty and the scatter in best-fitting α. The standard deviations are found to be somewhat larger than the mean uncertainties, likely due to the fact that the likelihoods are non-Gaussian. These results suggest that, generally, we can trust the individual likelihoods (more so than, e.g. taking the mean shape and width of the likelihood of the mocks), especially in the cases with the best apparent signal-to-noise ratio.

The results of this section can be summarized as follows: the $w(\theta)$ results are the least biased; their bias is only at a 2.3σ level, when considering the combined precision of all 1800 mocks, and at least part of the this bias can be explained by the positive bias expected from non-linear structure growth. The C_ℓ and ξ results are each biased at more than 5σ, based on the combined precision of all of the mocks. The ξ results are the most precise of any method and are the most likely to obtain a detection. Combining either the ξ or C_ℓ statistics with the $w(\theta)$ results can produce small improvements in the precision at the cost of increasing the bias in the α measurement. We determine this increased bias is unlikely to be worth the gain in precision, but leave any final determinations to be based on analysis of the DES Y1 data.

5 RESULTS

Here, we focus only on the BAO signal. The validation of the full shape of the clustering signal of the DES Y1 BAO sample is presented in DES-BAO-MOCKS and DES-BAO-SAMPLE. DES-BAO-MOCKS shows that both the angular and $\xi(s_\perp)$ clustering measurements agree well with the clustering in the mock samples. DES-BAO-SAMPLE shows that the clustering is well matched to expectations of linear theory in all of our redshift bins and that the galaxy bias evolves from approximately 1.8–2.0 within our $0.6 < z < 1.0$ redshift range. DES-BAO-SAMPLE also shows that the impact from observational systematics, determined by comparing the clustering with and without the systematics weights, is small. We refer the reader to DES-BAO-SAMPLE for clustering measurements where the non-BAO information is included. Harmonic space measurements and interpretation are presented in DES-BAO-ℓ-METHOD. We present the configuration space DES Y1 BAO signal, determined by subtracting the 'no wiggle' component [see equation (17) and surrounding discussion] of the best-fitting model

(labelled as 'noBAO' in figures). We present the DES Y1 measurements of the angular diameter distance to $z = 0.81$ in the following subsection and describe the series of robustness tests we apply to the data in Section 5.2.

5.1 BAO measurements

Here, we present the best-fitting BAO results and likelihoods. Table 5 lists our BAO measurements for the DES Y1 data and robustness tests on these data. We find similar results for $w(\theta)$ and $\xi(s_\perp)$, both in terms of α and its uncertainty. Fig. 2 displays these results for our DES Y1 data using orange stars for $0.6 < z < 1.0$ and yellow stars for $0.7 < z < 1.0$. Clearly, our results are consistent within the expected scatter.

Fig. 4 displays the BAO signal we measure in $w(\theta)$. To make this plot, we have subtracted the model obtained when using the same best-fitting parameters but using the smooth $w(\theta)_{\rm noBAO}$ template (obtained from $P_{\rm nw}$). In order to plot each redshift bin clearly, we have added significant vertical offsets (and some small horizontal ones). One can see that the BAO feature in the model moves to lower values of θ as the redshift increases, as the comoving location of the BAO feature is constant. Such a pattern is observed in the data for $z > 0.7$. The combination of these four $w(\theta)$ measurements, accounting for the covariance between the redshift bins, yields a measurement of $\alpha = 1.031 \pm 0.041$, i.e. approximately a 3 per cent greater angular diameter distance than predicted by our fiducial cosmology, but with 4 per cent uncertainty. The overall fit to the DES Y1 data is acceptable, as a $\chi^2 = 53$ for 43 degrees of freedom has a p-value of 0.14. Despite its appearance, the $0.6 < z < 0.7$ does not have a substantial effect on the goodness of fit; as the best fit has a $\chi^2/{\rm dof} = 37/32$ when these data are removed.

Fig. 5 displays the Y1 BAO feature, isolated in harmonic space and compared to the best-fitting model. This figure is analogous to Fig. 4 for $w(\theta)$. Here, we see that the BAO feature in the model moves towards higher ℓ as the redshift increases and that this behaviour is traced by the data points. In harmonic space we find $\alpha = 1.023 \pm 0.047$, which is a shift in α of approximately 0.25σ compared to the $w(\theta)$ measurement and slightly greater uncertainty for C_ℓ. As shown in Fig 3, such differences are typical for the mock results. We are therefore satisfied with the agreement between configuration and harmonic space results. The $\chi^2/{\rm dof} = 94/63$ we obtain for the C_ℓ fit is slightly high. The formal p-value is 0.007, suggesting that the result is unlikely. Using an analytic covariance matrix (denoted 'alt. cov' in Table 5) instead of the one derived from mocks reduces the $\chi^2/{\rm dof} = 86/63$, with a p-value of 0.029 and shifts the result to $\alpha = 1.039 \pm 0.053$. The combination of a significant bias on the results recovered from the mock analysis and the poor χ^2 recovered from the fits to the DES Y1 data make us discount the use of the C_ℓ results as representing the signal in the DES Y1 data. However, the agreement with the $w(\theta)$ is encouraging as a robustness test and we expect future studies to make further use of the C_ℓ results given future methodological improvements. Further tests of the C_ℓ results can be found in DES-BAO-ℓ-METHOD.

Fig. 6 displays the DES Y1 BAO signal in $\xi(s_\perp)$ using $0.6 < z < 1.0$, again by subtracting the no BAO component of the best-fitting model. This represents the result listed as 'fiducial' in Table 5. The $\chi^2 = 9$ for 9 dof. This result is chosen as the fiducial result ξ (from among four choices of bin centre) as it has very similar signal-to-noise ratio and best-fitting value as the $w(\theta)$ result, which we will use for our DES Y1 measurement, and thus represents a highly compressed illustration of the DES Y1 BAO signal. The ξ result we quote as 'combined' in Table 5 is obtained from the mean

Table 5. Results for BAO fits to the Y1 data. The top line quotes our consensus DES Y1 result from $w(\theta)$ in terms of the physical distance ratio $D_{\rm A}(z = 0.81)/r_{\rm d}$. The other lines report measurements of α, which represent the measured shift in $D_{\rm A}(z = 0.81)/r_{\rm d}$ relative to our fiducial MICE cosmology; e.g. the value expected for *Planck* ΛCDM is $\alpha = 1.042$. All results assume a flat prior $0.8 < \alpha < 1.2$. Robustness tests against our fiducial analysis settings are reported. These settings include: we use the full $0.6 < z < 1.0$ data set; the binning in $w(\theta)$ is 0.3 deg and its range is $0.5 < \theta < 5$ deg; the binning in ξ is $\Delta s_\perp = 12\,h^{-1}$ Mpc, the range of included bin centres is $30 < s_\perp < 200\,h^{-1}$ Mpc, and the first included bin centre allows pairs with $27 < s_\perp < 39\,h^{-1}$ Mpc. The 'bins combined' ξ result is derived from the mean likelihood of the fiducial result and three additional bin centres, shifted in steps of $3\,h^{-1}$ Mpc (and each individual result is denoted below by $+/-x$). 'BPZ' denotes that the BPZ photozs were used, as opposed to the fiducial DNF and 'z uncal' refers to the case where we use the redshift distribution reported by DNF without any additional calibration for determining the theoretical template. For cases where we alter the assumed $\Sigma_{\rm nl}$ in the template, the units of the quoted values are h^{-1} Mpc; the fiducial values are $8\,h^{-1}$ Mpc for ξ and $5.2\,h^{-1}$ Mpc for $w(\theta)$ and C_ℓ. '*Planck*' denotes the case where a cosmology consistent with *Planck* ΛCDM has been used to calculate paircounts and the BAO template. $A = 0$ denotes that no broad-band polynomial was used in the fit, while $a_{\rm x}$ denotes variations on the terms that were included.

Y1 measurement	$D_{\rm A}/r_{\rm d}$	
$z_{\rm eff} = 0.81$	10.75 ± 0.43	
Case	α	χ^2/dof
$w(\theta)$ [Y1 choice]	1.033 ± 0.041	53/43
Robustness tests:		
C_ℓ	1.023 ± 0.047	94/63
C_ℓ alt cov.	1.039 ± 0.053	86/63
$w(\theta)$ fiducial	1.033 ± 0.041	53/43
$w(\theta)$ $\Delta\theta = 0.15$	1.033 ± 0.045	159/103
$w(\theta)$ $\theta_{\rm min} = 1$	1.038 ± 0.038	50/39
$w(\theta)$ *Planck*$\times$1.042	1.034 ± 0.043	44/43
$w(\theta)$ BPZ	1.018 ± 0.043	56/43
$w(\theta)$ z uncal	1.023 ± 0.040	52/43
$w(\theta)$ no $w_{\rm sys}$	1.028 ± 0.039	51/43
$w(\theta)$ $\Sigma_{\rm nl} = 2.6$	1.028 ± 0.035	51/43
$w(\theta)$ $\Sigma_{\rm nl} = 7.8$	1.033 ± 0.056	55/43
$w(\theta)$ free $\Sigma_{\rm nl}$	1.028 ± 0.033	51/42
$w(\theta)$ $0.7 < z < 1.0$	1.053 ± 0.040	37/32
$w(\theta)$ $A = 0$	1.030 ± 0.040	59/55
$w(\theta)$ Gaussian cov.	1.038 ± 0.033	88/43
ξ (bins combined)	1.026 ± 0.044	9/9
ξ fiducial binning	1.031 ± 0.040	9/9
ξ -3	1.031 ± 0.045	12/9
ξ $+3$	1.017 ± 0.041	8/9
ξ $+6$	1.025 ± 0.050	7/8
ξ $\Delta s_\perp = 5$	1.021 ± 0.041	45/29
ξ $\Delta s_\perp = 8$	1.029 ± 0.046	31/16
ξ $\Delta s_\perp = 10$	1.022 ± 0.037	16/12
ξ $\Delta s_\perp = 15$	1.012 ± 0.039	7.5/6
ξ $s_{\perp,{\rm min}} = 50$	1.032 ± 0.046	8/7
ξ *Planck*$\times$1.042	1.018 ± 0.041	7/9
ξ BPZ	1.012 ± 0.040	12/9
ξ no $w_{\rm sys}$	1.029 ± 0.040	10/9
ξ $\Sigma_{\rm nl} = 4$	1.023 ± 0.038	9/9
ξ $\Sigma_{\rm nl} = 12$	1.043 ± 0.052	11/9
ξ $\Sigma_{\rm nl}$ free	1.024 ± 0.039	9/9
ξ $A = 0$	1.039 ± 0.040	10/12
ξ $0.7 < z < 1.0$	1.052 ± 0.031	17/9

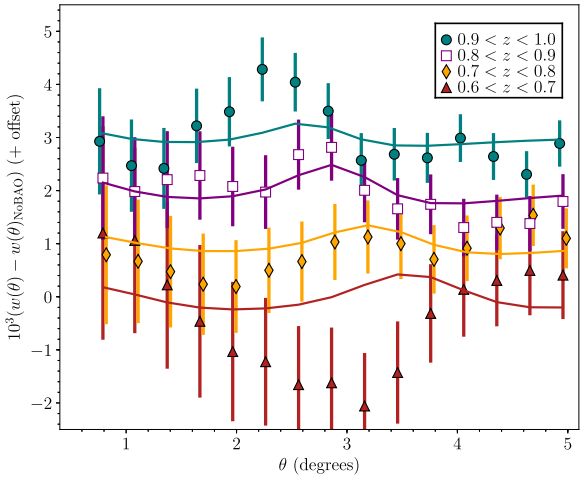

Figure 4. The BAO signal in DES Y1 clustering, observed in the angular autocorrelation, $w(\theta)$ and isolated by subtracting the no BAO component of the best-fitting model. The result has been multiplied by 10^3 and we add vertical offsets of 0, 1, 2, and 3 sequentially with redshift. The θ values have been shifted by 0.03 for the $0.7 < z < 0.8$ and by –0.03 for the $0.9 < z < 1.0$ redshift bins. The BAO feature moves to lower θ at higher redshift, as it has the same comoving physical scale. The signal from these redshift bins is combined, accounting for the covariance between them, in order to provide a 4 per cent angular diameter distance measurement at the effective redshift of the full sample. Neighbouring data points are strongly correlated. The total χ^2/dof (including all cross-covariance between redshift bins) is 53/43 and other studies show that, despite its appearance, the $0.6 < z < 0.7$ bin has a $\chi^2/{\rm dof} \sim 1$.

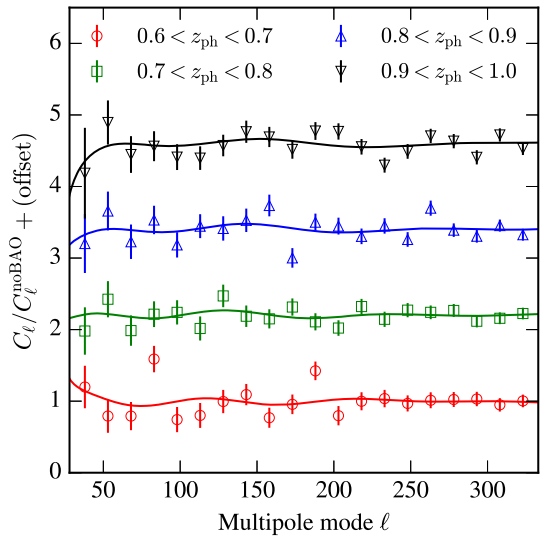

Figure 5. The measured Y1 BAO feature, same as Fig. 4, but isolated in spherical harmonic space. From top to bottom, one can see that the BAO feature moves to the left, towards lower ℓ, reflecting the redshift evolution of a feature of constant comoving size.

likelihood of four ξ results, each using a bin size of 12 h^{-1} Mpc with the bin size shifted in increments of 3 h^{-1} Mpc; this procedure of taking the mean across the bin centres was demonstrated to slightly improve the results for mock data in Section 4. This result is similar to the $w(\theta)$ result, with a slightly greater uncertainty. Comparing the orange stars to the white circles in Fig 2 indicates that the differences we find in the $w(\theta)$ and $\xi(s_\perp)$ results are typical.

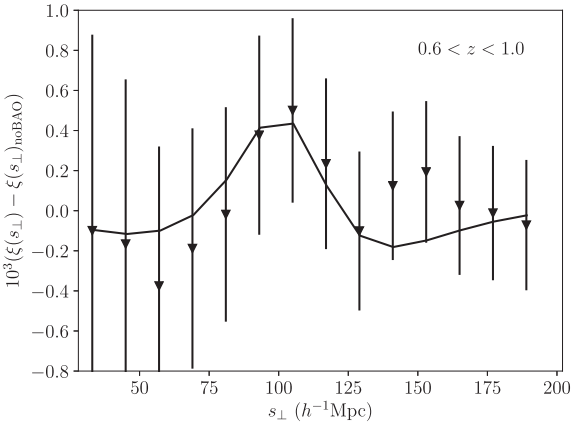

Figure 6. The BAO signal in DES Y1 clustering, observed in the auto-correlation binned in projected physical separation, $\xi(s_\perp)$, and isolated by subtracting the no BAO component of the best-fitting model. Neighbouring data points are strongly correlated.

We recover, for both $w(\theta)$ and $\xi(s_\perp)$, a smaller uncertainty when we ignore the $0.6 < z < 0.7$ data; i.e. the signal-to-noise ratio appears greater in the $0.7 < z < 1.0$ sample than for the $0.6 < z < 1.0$ data. This is, of course, unexpected. In Appendix A, we compare results obtained from mock realizations using both redshift ranges. We find that eight per cent of the realizations obtain an uncertainty that is improved by a greater factor than we find for DES Y1 when ignoring the $0.6 < z < 0.7$ data (and 30 per cent satisfy the condition that the $0.7 < z < 1.0$ uncertainty is less than the $0.6 < z < 1.0$ uncertainty). This eight per cent becomes more significant when one considers that to truly consider how likely the result is, we would have to test removing all independent equal-sized volumes, not just those with $0.6 < z < 0.7$. These eight per cent of cases are thus not particularly unusual. Studying them further, we find that the $0.6 < z < 1.0$ results are more trustworthy, but the uncertainty on α is likely overestimated. Thus, we use the full $0.6 < z < 1.0$ data set for our DES Y1 result as this is the more conservative choice. A final decision to be made is how to treat the $w(\theta)$ and $\xi(s_\perp)$ results. Given that the $w(\theta)$ results are more precise in the $0.6 < z < 1.0$ redshift range, are less biased when tested on the mock samples, and are less dependent on the choice of damping scale (see the next subsection), we use the $w(\theta)$ results as our choice for the DES Y1 measurement.

Fig. 7 displays the $\Delta\chi^2$ likelihood for α using $w(\theta)$ and $\xi(s_\perp)$. The dashed line is for the no BAO model (derived from $P_{\rm nw}$). We find a preference for BAO that is greater than 2σ for both $w(\theta)$ and $\xi(s_\perp)$. The $w(\theta)$ and $\xi(s_\perp)$ likelihoods are close near the maximum likelihood, but diverge at high α values. Thus, our $\Delta\chi^2 = 1$ definition for α and its uncertainty recovers results that agree quite well. A summary of the differences is that ξ rejects low α with slightly greater significance and $w(\theta)$ rejects high α with greater significance. We use the full $w(\theta)$ likelihood for any cosmological tests, as the Gaussian approximation is clearly poor outside of the $\sim 1\sigma$ region.

5.2 Robustness tests

We vary our methodology in a variety of ways in order to test the robustness of our results. We have already shown that ξ and $w(\theta)$ obtain consistent results and that the change in results when eliminating $0.6 < z < 0.7$ data are consistent with expectations

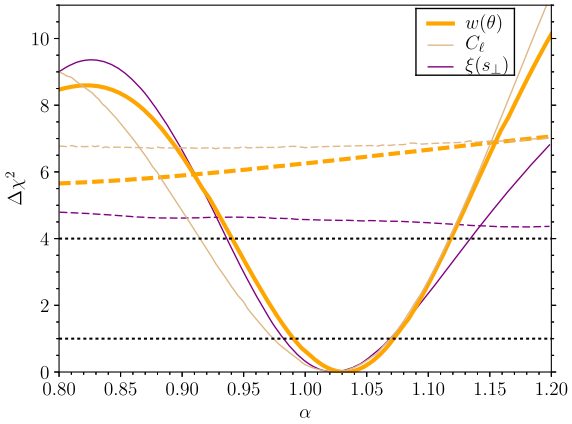

Figure 7. The BAO likelihood for DES Y1 data, for $w(\theta)$, C_ℓ, and $\xi(s_\perp)$. The dashed line shows the result for a model with no BAO, indicating that the data prefers a BAO feature at greater than 2σ significance. The dotted black lines denote 1σ and 2σ, based on $x\sigma = \sqrt{\Delta\chi^2}$.

based on tests on mock realizations. Here, we consider how the results change with different modelling assumptions, changes in the range of scales used, the bin size, the use of the systematic weights, the choice of photometric redshifts, and if a harmonic-space estimator is used instead of the configuration space ones. The results are tabulated in the bottom rows of Table 5.

One significant concern in our work is the use of photometric redshifts. Throughout, we have assumed the fiducial $\phi(z_{\rm true})$ results obtained from the redshift validation described in DES-BAO-SAMPLE are correct. However, the impact of this validation on our recovered results is relatively small. The output of DNF provides an initial estimate of the redshift distribution, which we also used to produce $w(\theta)$ BAO templates. Using these BAO templates, labelled 'z uncal' in Table 5, our measurement by only 0.25σ towards a smaller α value. This test performed only for $w(\theta)$, but given that the main effect is simply to shift the mean redshifts assumed in the analysis, we expect similar results for the other statistics. Further, this test presents the results obtained with no attempt to calibrate the photometric redshifts and instead simply stacking the output from the redshift pipeline. It shows that our results shift by only a fraction of a σ. The redshift validation produces more accurate determinations of the redshift distributions. The estimated uncertainties in the mean redshift obtained from the process are less than 0.8 per cent at all redshifts, i.e. $\sigma(\bar{z})/\bar{z} < 0.008$. The effect on the BAO measurement can be approximated as this being a constant shift in all redshifts and this affects each clustering estimator equally. This converts to a systematic uncertainty on our α measurement of 0.006. This is 15 per cent of our statistical uncertainty and thus negligible for this DES Y1 analysis. More detailed tests are shown in DES-BAO-θ-METHOD.

An additional test of the robustness to redshift uncertainties is to use a different method, BPZ, to estimate the photometric redshifts and reproduce the sample and measurements. For this test, we still use the covariance obtained from the fiducial 1800 mock realizations with redshift distributions matched to our fiducial DNF photometric redshifts. However, the BAO templates for the measurements are produced using the BPZ redshift distributions estimated through their redshift validation. As for DNF, we find similar results for $w(\theta)$ and ξ, as each shifts to a slightly smaller value of α. This is a 0.32σ shift for ξ and 0.37σ for $w(\theta)$. For $w(\theta)$, this is the level of shift expected if the two samples have a correlation, c, of 0.93 (calculated via $\sigma = \sqrt{2-2*c}$). Given that only 88 per cent of the galaxies used are the same (it is less than 100 per cent because galaxies scatter across the redshift boundaries) and the number of matches per $\Delta z = 0.1$ redshift bin is at most 56 per cent, we are confident the expected correlation in BAO results obtained from the two redshift estimates is less than 0.93. We therefore conclude the differences in the results between the two redshift estimates are not statistically significant.

The damping scale that we assume in our BAO template affects our results, mostly in terms of the recovered uncertainty for $w(\theta)$ (which we use for our Y1 measurement). For both $w(\theta)$ and ξ, we test both halving our fiducial scale and making it 50 per cent greater. This change is far greater than the change expected between our fiducial cosmology and that of Planck Collaboration et al. (2016). For $w(\theta)$, using the low damping scale shifts α lower by 0.005 (0.12σ) and decreases the uncertainty by 15 per cent. Using the greater damping scale does not shift α but increases the uncertainty by 37 per cent. The data slightly prefer the lower damping scale, as $\Delta\chi^2 = 2$ compared to the fiducial case. Allowing the damping to be free has a best fit at low $\Sigma_{\rm nl}$ values and thus significantly reduces the uncertainty but shifts α (lower) by only 0.12σ. Thus, the distance obtained from our $w(\theta)$ results used for our DES Y1 measurement is robust to the choice of damping scale. The uncertainty on the measurement depends fairly strongly on how the damping scale is treated, and we thus choose to use the damping scale that is best fit to our mock samples, $\Sigma_{\rm nl} = 5.2\,h^{-1}$ Mpc, which is close to theoretical expectations.

For $\xi(s_\perp)$, we find a similar effect on the uncertainty and greater shifts in the recovered α. The α values shift by $\sim\pm\,0.25\sigma$. Allowing $\Sigma_{\rm nl}$ to be a free parameter yields a result that is close to the result for $\Sigma_{\rm nl} = 4\,h^{-1}$ Mpc, as, similar to $w(\theta)$, the DES Y1 data slightly prefer the smaller damping scale. Thus, marginalizing over $\Sigma_{\rm nl}$ results in a smaller estimated uncertainty. Therefore, as with $w(\theta)$, we choose to use the results with the fixed damping scale as our measurement. However, for the DES Y1 data set, the $\xi(s_\perp)$ results are not as robust to the choice of damping value as $w(\theta)$, which is one of the reasons we use the $w(\theta)$ results as our choice for the DES Y1 measurement.

When ignoring the systematic weights, we find almost no change in the recovered BAO measurements. The change is greatest for $w(\theta)$, but only 0.13σ. This is consistent with results from spectroscopic surveys (Ross et al. 2017a; Ata et al. 2017), which have consistently demonstrated that BAO measurements are robust to observational systematic effects. Additionally, no large deviations are found when the bin size or range of scale fit are changed. Finally, there is no significant change in our results if we set the broad-band polynomial terms to 0, denoted by '$A = 0$' in Table 5.

As a final test, we obtain results when we assume a cosmology consistent with *Planck* ΛCDM (Planck Collaboration et al. 2016) for calculating both the pair counts and BAO template. For this, we use the same fiducial cosmology recently assumed in Alam et al. (2016), which is flat ΛCDM with $\Omega_{\rm matter} = 0.31$, $h = 0.676$, and $\Omega_{\rm baryon}\,h^2 = 0.022$. When using this cosmology, we expect to obtain an α-value that is lower by 1.042, thus in Table 5 we have multiplied the *Planck* results by 1.042. For ξ, the shift is 0.008 in α (0.18σ) away from the combined result using the MICE cosmology. For ξ, we expect a difference similar to what was found for the bin centre tests, as the pair counts were recalculated assuming the *Planck* cosmology; our result is only slightly greater than the variance associated with alternative binnings. For $w(\theta)$, the results using the

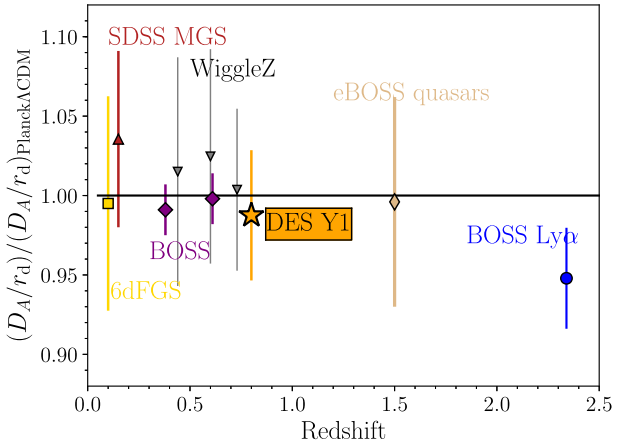

Figure 8. Measurement of the angular diameter distance measured from BAO, compared to the *Planck* ΛCDM prediction. The DES Y1 measurement is shown using a gold star. The additional measurements are described in the text. Where possible, we have used the available D_A measurement. Some studies have reported only spherically averaged distances; in these cases we have multiplied the uncertainty by 1.5 (as this is the approximate scaling between spherically averaged and transverse signal-to-noise ratio). The results where this scaling was applied are 6dFGS, SDSS MGS, and eBOSS quasars.

Planck template are nearly identical to those using the default MICE template as all differences are within 0.002. For $w(\theta)$, we also alter the covariance matrix so that the Gaussian part is given by the Planck Collaboration et al. (2016) cosmology, using equation (14). Thus, we conclude the choice of fiducial cosmology has a negligible effect on our results.

6 COSMOLOGICAL CONTEXT

Our DES Y1 BAO measurement can be used to constrain cosmological models, given the likelihood for α (shown in Fig. 7), our fiducial cosmology, and the effective redshift of our measurement. This requires multiplying the α measurements by $\frac{D_A^{\rm fid}(z_{\rm eff})}{r_d^{\rm fid}} = 10.41$ and testing this against the $\frac{D_A(z_{0.81})}{r_d}$ predicted by any given cosmological model.[5] In the top row of Table 5, we have thus multiplied the $w(\theta)$ results by 10.41 in order to quote our Y1 measurement of $\frac{D_A(z_{0.81})}{r_d} = 10.75 \pm 0.43$.

Fig. 8 displays our measurement, compared to other BAO angular diameter distance measurements and the *Planck* ΛCDM prediction (with fixed minimal neutrino mass). We include measurements from Beutler et al. (2011, 6dFGS), Ross et al. (2015a, SDSS MGS), Alam et al. (2016, SDSS-III Baryon Oscillation Spectroscopic Survey (BOSS)), Kazin et al. (2014,WiggleZ), Ata et al. (2017, eBOSS quasars), and the combination of Bautista et al. (2017a) and du Mas des Bourboux et al. (2017, BOSS Lyα). These make up the most up to date, and largely independent, BAO distance ladder. Many of the BAO measurements were made in terms of the spherically averaged distance quantity, which is a combination of the angular diameter distance and $H(z)$. Assuming spherical symmetry, the $D_A(z)$ constraints are 50 per cent less precise (Ross et al. 2015b) and we have thus multiplied the error bars by 1.5, while fixing the relative $(D_A/r_d)/(D_A/r_d)_{\rm Planck\Lambda CDM}$ value to be the same as for spherically averaged measurement.

The DES Y1 measurement is consistent with expectations from *Planck* ΛCDM and previous BAO measurements. While the new measurement is not nearly as precise as BOSS measurements, it is the most precise D_A measurement in the range $0.6 < z < 2$. The DES Y1 and the 6dFGS (yellow square) are the only measurements displayed that do not rely on imaging from SDSS. The DES measurement is the only one that does not rely on spectroscopic redshifts. The precision of our measurement is similar to that obtained previously at $z \sim 0.55$ by the combination of Crocce et al. (2011) and Carnero et al. (2012) and independently Seo et al. (2012) using SDSS imaging data and photometric redshifts (not plotted).

We can also compare with the recent DES Y1 results obtained in DES Collaboration et al. 2017 (hereafter 'DES 3x2pt'). Converting the results from the DES 3x2pt ΛCDM Monte Carlo Markov Chains to a posterior likelihood for $D_A(0.81)/r_d$, we obtain 10.59 ± 0.44. Thus, our DES Y1 BAO measurement is in agreement with the results of DES 3x2pt assuming the ΛCDM model.

7 CONCLUSIONS

The results of this study can be summarized as follows:

(i) We have used a sample of 1.3 million DES Y1 galaxies spread over 1336deg^2 with $0.6 < z_{\rm photo} < 1.0$, defined in Crocce et al. (2017, DES-BAO-SAMPLE), in order to obtain a 4 per cent measurement of the ratio of the angular diameter distance to $z = 0.81$ to the size of the BAO standard ruler set by early Universe recombination physics: $D_A(z_{\rm eff} = 0.81)/r_d = 10.75 \pm 0.43$.

(ii) In order to construct covariance matrices and set analysis choices, we have used 1800 mock realizations of the DES Y1 sample, constructed as described in Avila et al. (2018, DES-BAO-MOCKS). Our DES Y1 results are typical given the distribution of recovered from the 1800 mock realizations.

(iii) We have used three separate projected clustering statistics, one defined in terms of the angular separation ($w(\theta)$, with methodology described in Chan et al. 2018; DES-BAO-θ-METHOD), another defined in terms of the projected physical separation ($\xi(s_\perp)$, with methodology described in Ross et al. 2017b; DES-BAO-$s_\perp$-METHOD), and a third in spherical harmonic space (C_ℓ, with methodology described in Camacho et al. 2018; methodcl). Each statistic returns consistent results (the difference is 0.25σ in the best-fitting value and the uncertainties differ by less than 15 per cent). These differences are consistent with differences found in the mock realizations. The preference for a BAO feature in the data is greater than 2σ for both clustering statistics. We use the $w(\theta)$ result as our consensus DES Y1 measurement, as its methodology was demonstrated to be most accurate when testing against mocks and it was more robust when testing the results obtained from various treatment of the DES Y1 data.

(iv) We obtain results using two photometric redshift estimates, one machine-learning based (DNF) and the other template based (BPZ), and obtain results that are matched to within 0.37σ. The DES Y1 results are based on the DNF results, which are the most precise and accurate as described, along with their validation in DES-BAO-SAMPLE. The results from the validation suggest that uncertainties in the accuracy of the DNF redshifts contribute a negligibly small systematic uncertainty to our DES Y1 BAO measurements.

(v) We find no significant changes in the $w(\theta)$ BAO measurements when varying the methodology, including omitting correc-

[5]We will make our likelihood publicly available after this work has been accepted for publication by the journal.

tions for observational systematics and using a different fiducial cosmology.

In short, we find our DES Y1 BAO measurement is robust to a number of stress tests and is consistent with our simulations of the DES Y1 data set. These results are the first BAO measurement obtained from DES. DES year three (Y3) data has already been observed and occupies the full 5000 deg^2 with greater average coverage in the number of exposures than Y1 over our 1336 deg^2. With these data, we expect to obtain results with approximately a factor of two smaller statistical uncertainty in the near future.

As a byproduct of the preparation for this analysis we have identified a number of items where improvement or further study will benefit DES Y3 measurements:

(i) Include a more realistic modelling of photometric redshift errors in the template of $\xi(s_\perp)$, which currently assumes Gaussian errors, which we believe are the reason for the systematic bias of 0.13σ when using that statistics, as discussed in Section 4.1 and shown in Table 3.

(ii) Reduce the uncertainty in the mean of the redshift distributions, which currently represents a systematic uncertainty of 0.15σ, see Section 5.2; this is the greatest of any systematic uncertainty we have identified that affects $w(\theta)$ results.

(iii) Revisit the theoretical template for the C_ℓ methodology, or otherwise pin down the cause of the biases shown in Table 3.

(iv) Further investigate the dependence of the covariance matrix on cosmological parameters and other choices (e.g. the type of mock used).

Altogether, based on our results, none of the above items will lead to systematic uncertainties close to the future level of statistical precision.

We expect our work can be used as a guide for future imaging surveys such as the Large Synoptic Survey Telescope (LSST; LSST Science Collaboration 2009). In turn, BAO measurements had previously been proven to be a robust and precise method for measuring cosmological distances when using spectroscopic redshifts (Alam et al. 2016, and references therein). We have obtained a similar level of robustness using a purely photometric data set. Based on this work, we expect DES Y3 data to provide the most precise BAO angular diameter distance measurement, excluding BOSS galaxy results. Further, the increased photometric depth of the Y3 and then final DES data will allow extensions to higher redshifts than probed here. Thus, together with emission-line galaxy data from the extended Baryon Oscillation Spectroscopic Survey (eBOSS; Dawson et al. 2016; comparable precision is expected), these data will be the first to use galaxies beyond redshift 1 to measure BAO. These measurements will thus pave the way for those obtained by the Dark Energy Spectroscopic Instrument (DESI Collaboration et al. 2016a,b) and *Euclid* (Laureijs et al. 2011; Amendola et al. 2013).

ACKNOWLEDGEMENTS

AJR is grateful for support from the Ohio State University Center for Cosmology and AstroParticle Physics. MC acknowledges support from the Spanish Ramon y Cajal MICINN program. KCC acknowledges the support from the Spanish Ministerio de Economia y Competitividad grant ESP2013-48274-C3-1-P and the Juan de la Cierva fellowship. NB acknowledges the use of University of Florida's supercomputer HiPerGator 2.0 as well as thanks the University of Florida's Research Computing staff. HC is supported by The Brazilian Conselho Nacional de Desenvolvimento Cientifíco e Tecnológico (CNPq). ML and RR are partially supported by the Sao Paulo Research Foundation (FAPESP) and CNPq. We are thankful for the support of the Instituto Nacional de Ciência e Tecnologia (INCT) e-Universe (CNPq grant 465376/2014-2).

This work has made use of CosmoHub, see Carretero et al. (2017). CosmoHub has been developed by the Port d'Informació Científica, maintained through a collaboration of the Institut de Física d'Altes Energies (IFAE) and the Centro de Investigaciones Energéticas, Medioambientales y Tecnológicas (CIEMAT), and was partially funded by the 'Plan Estatal de Investigación Cientfica y Técnica y de Innovación' program of the Spanish government.

We are grateful for the extraordinary contributions of our CTIO colleagues and the DECam Construction, Commissioning and Science Verification teams in achieving the excellent instrument and telescope conditions that have made this work possible. The success of this project also relies critically on the expertise and dedication of the DESDM group.

Funding for the DES Projects has been provided by the U.S. Department of Energy, the U.S. National Science Foundation, the Ministry of Science and Education of Spain, the Science and Technology Facilities Council of the United Kingdom, the Higher Education Funding Council for England, the National Center for Supercomputing Applications at the University of Illinois at Urbana-Champaign, the Kavli Institute of Cosmological Physics at the University of Chicago, the Center for Cosmology and Astro-Particle Physics at the Ohio State University, the Mitchell Institute for Fundamental Physics and Astronomy at Texas A&M University, Financiadora de Estudos e Projetos, Fundação Carlos Chagas Filho de Amparo à Pesquisa do Estado do Rio de Janeiro, Conselho Nacional de Desenvolvimento Científico e Tecnológico and the Ministério da Ciência, Tecnologia e Inovação, the Deutsche Forschungsgemeinschaft, and the Collaborating Institutions in the DES.

The Collaborating Institutions are Argonne National Laboratory, the University of California at Santa Cruz, the University of Cambridge, Centro de Investigaciones Energéticas, Medioambientales y Tecnológicas-Madrid, the University of Chicago, University College London, the DES-Brazil Consortium, the University of Edinburgh, the Eidgenössische Technische Hochschule (ETH) Zürich, Fermi National Accelerator Laboratory, the University of Illinois at Urbana-Champaign, the Institut de Ciències de l'Espai (IEEC/CSIC), the Institut de Física d'Altes Energies, Lawrence Berkeley National Laboratory, the Ludwig-Maximilians Universität München and the associated Excellence Cluster Universe, the University of Michigan, the National Optical Astronomy Observatory, the University of Nottingham, The Ohio State University, the University of Pennsylvania, the University of Portsmouth, SLAC National Accelerator Laboratory, Stanford University, the University of Sussex, Texas A&M University, and the OzDES Membership Consortium.

Based in part on observations at Cerro Tololo Inter-American Observatory, National Optical Astronomy Observatory, which is operated by the Association of Universities for Research in Astronomy (AURA) under a cooperative agreement with the National Science Foundation.

The DESDM system is supported by the National Science Foundation under grant numbers AST-1138766 and AST-1536171. The DES participants from Spanish institutions are partially supported by MINECO under grants AYA2015-71825, ESP2015-66861, FPA2015-68048, SEV-2016-0588, SEV-2016-0597, and MDM-2015-0509, some of which include ERDF funds from the European Union. IFAE is partially funded by the CERCA program of the Generalitat de Catalunya. Research leading to these results

has received funding from the European Research Council under the European Union's Seventh Framework Program (FP7/2007-2013) including ERC grant agreements 240672, 291329, and 306478. We acknowledge support from the Australian Research Council Centre of Excellence for All-sky Astrophysics, through project number CE110001020.

This manuscript has been authored by Fermi Research Alliance, LLC under contract no. DE-AC02-07CH11359 with the U.S. Department of Energy, Office of Science, Office of High Energy Physics. The United States Government retains and the publisher, by accepting the article for publication, acknowledges that the United States Government retains a non-exclusive, paid-up, irrevocable, world-wide license to publish or reproduce the published form of this manuscript, or allow others to do so, for United States Government purposes.

REFERENCES

Alam S. et al., 2016, MNRAS, 470, 2617
Amendola L. et al., 2013, Living Rev. Relativ., 16, 6
Anderson L. et al., 2014, MNRAS, 441, 24
Ata M. et al., 2017, MNRAS, 473, 4773
Avila S. G., Murray S., Knebe A., Power C., Robotham A. S., Garcia-Bellido J., 2015, MNRAS, 450, 1856
Avila S. et al., 2018, MNRAS, 479, 94
Bautista J. E. et al., 2017, A&A, 603, A12
Bautista J. E. et al., 2018, ApJ, 863, 110
Benítez N., 2000, ApJ, 536, 571
Beutler F. et al., 2011, MNRAS, 416, 3017
Blake C., Bridle S., 2005, MNRAS, 363, 1329
Blake C. et al., 2011, MNRAS, 415, 2892
Camacho H. et al., 2018, preprint (arXiv:1807.10163)
Carnero A., Sánchez E., Crocce M., Cabré A., Gaztañaga E., 2012, MNRAS, 419, 1689
Carretero J., Castander F. J., Gaztañaga E., Crocce M., Fosalba P., 2015, MNRAS, 447, 646
Carretero J. et al., 2017, Proceedings of the European Physical Society Conference on High Energy Physics (EPS-HEP2017). Venice, Italy
Chan K. C. et al., 2018, MNRAS, 480, 3031
Cole S. et al., 2005, MNRAS, 362, 505
Crocce M., Scoccimarro R., 2008, Phys. Rev. D, 77, 023533
Crocce M., Gaztañaga E., Cabré A., Carnero A., Sánchez E., 2011, MNRAS, 417, 2577
Crocce M., Castander F. J., Gaztañaga E., Fosalba P., Carretero J., 2015, MNRAS, 453, 1513
Crocce M. et al., 2017, MNRAS, 482, 2807
Dawson K. S. et al., 2016, AJ, 151, 44
De Vicente J., Sánchez E., Sevilla-Noarbe I., 2016, MNRAS, 459, 3078
Delubac T. et al., 2015, A&A, 574, A59
DES Collaboration, 2017, preprint (arXiv:1708.01530)
Desai S. et al., 2012, ApJ, 757, 83
DESI Collaboration, 2016a, preprint (arXiv:1611.00036)
DESI Collaboration, 2016b, preprint (arXiv:1611.00037)
Diehl H. T. et al., 2014, Proc. SPIE, 9149, 91490V
Dodelson S., Schneider M. D., 2013, Phys. Rev. D, 88, 063537
Drlica-Wagner A. et al., 2017, A&A, 608, A130
du Mas des Bourboux H. et al., 2017, A&A, 608, A130
Eisenstein D. J. et al., 2005, ApJ, 633, 560
Eisenstein D. J., Hu W., 1998, ApJ, 496, 605
Elvin-Poole J. et al., 2017, Phys. Rev. D, 98, 042006
Estrada J., Sefusatti E., Frieman J. A., 2009, ApJ, 692, 265
Flaugher B. et al., 2015, ApJ, 150, 150
Fosalba P., Crocce M., Gaztañaga E., Castander F. J., 2015a, MNRAS, 448, 2987
Fosalba P., Gaztañaga E., Castander F. J., Crocce M., 2015b, MNRAS, 447, 1319
Gaztañaga E., Cabré A., Hui L., 2009, MNRAS, 399, 1663
Górski K. M., Hivon E., Banday A. J., Wandelt B. D., Hansen F. K., Reinecke M., Bartelmann M., 2005, ApJ, 622, 759
Hartlap J., Simon P., Schneider P., 2007, A&A, 464, 399
Hivon E., Gorski K. M., Netterfield C. B., Crill B. P., Prunet S., Hansen F., 2002, ApJ, 567, 2
Hütsi G., 2010, MNRAS, 401, 2477
Kaiser N., 1987, MNRAS, 227, 1
Kazin E. A. et al., 2014, MNRAS, 441, 3524
Labatie A., Starck J. L., Lachièze-Rey M., 2012, ApJ, 760, 97
Landy S. D., Szalay A. S., 1993, ApJ, 412, 64
Laureijs R. et al., 2011, preprint (arXiv:1110.3193)
Lewis A., Challinor A., Lasenby A., 2000, ApJ, 538, 473
LSST Science Collaboration, 2009, preprint (arXiv:0912.0201)
MacCrann N. et al., 2018, MNRAS, 480, 4614
Mohr J. et al., 2008, Proc. SPIE, 7016, 70160L
Morrison C. B., Schneider M. D., 2013, J. Cosmol. Astropart. Phys., 11, 009
Padmanabhan N., White M., 2009, Phys. Rev. D, 80, 063508
Padmanabhan N. et al., 2007, MNRAS, 378, 852
Percival W.J. et al., 2010, MNRAS, 401, 2148
Percival W. J. et al., 2001, MNRAS, 327, 1297
Percival W. J. et al., 2014, MNRAS, 439, 2531
Planck Collaboration 2016, A&A, 594, A13
Ross A. J. et al., 2017a, MNRAS, 464, 1168
Ross A. J., Samushia L., Howlett C., Percival W. J., Burden A., Manera M., 2015a, MNRAS, 449, 835
Ross A. J., Percival W. J., Manera M., 2015b, MNRAS, 451, 1331
Ross A. J. et al., 2017b, MNRAS, 472, 4456
Sánchez E. et al., 2011, MNRAS, 411, 277
Seo H.-J., Eisenstein D. J., 2003, ApJ, 598, 720
Seo H.-J., Eisenstein D. J., 2007, ApJ, 665, 14
Seo H.-J. et al., 2012, ApJ, 761, 13
Sevilla I. et al., 2011, preprint (arXiv:1109.6741)
Taylor A., Joachimi B., Kitching T., 2013, MNRAS, 432, 1928
Vargas-Magaña M. et al., 2018, MNRAS, 477, 1153
White M., Padmanabhan N., 2015, J. Cosmol. Astropart. Phys., 12, 058
Xu X., Padmanabhan N., Eisenstein D. J., Mehta K. T., Cuesta A. J., 2012, MNRAS, 427, 2146
Zhan H., Knox L., Tyson J. A., 2009, ApJ, 690, 923
Zhu F., Padmanabhan N., White M., 2015, MNRAS, 451, 236
Zhu F. et al., 2018, MNRAS, 480, 1096

APPENDIX A: COMPARISON BETWEEN $0.6 < z < 0.7$ AND $0.7 < z < 1.0$ RESULTS

As described in Section 5, we obtain more precise BAO measurements when excluding data with $0.6 < z < 0.7$. In this appendix, we use the mock realizations in order to assess how unusual this is and how best to treat the results in such a case. We compare the results of fitting to 1800 mock realizations without using the $0.6 < z < 0.7$ data compared to the full range. This is shown in Fig. A1. 1538 mock realizations (85 per cent) have a detection in both redshift ranges. As to be expected the results are strongly correlated. We see that the recovered uncertainty is usually greater when omitting the $0.6 < z < 0.7$, but this is not always the case. We find 130 (8 per cent) of the mock realizations recover an uncertainty $\sigma_1/\sigma_2 > 0.043/0.036$. The values $\sigma = 0.43$ and 0.36 represent the mean of the $w(\theta)$ and $\xi(s_\perp)$ uncertainties recovered from the DES Y1 data for the respective redshift ranges. Thus, our data measurement is not particularly unlikely in terms of this statistic, even without folding in the look-elsewhere effect, which would further decrease the significance because we are only considering a single anomalous statistic.

As can be seen based on the position of the orange star in the bottom panel of Fig. A1, the value of α shifts when removing the $0.6 < z < 0.7$ data, but remains within the locus of mock realization

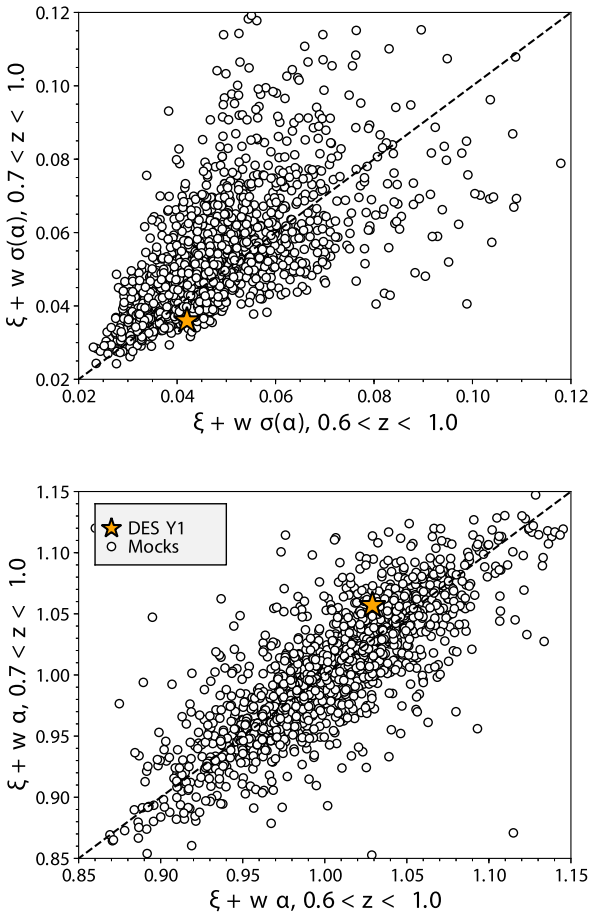

Figure A1. A comparison of $\xi + w$ BAO fit results when using the full $0.6 < z < 1.0$ redshift range and one restricted to $0.7 < z < 1.0$.

results. In order to quantify the shift, we consider $|\alpha_1 - \alpha_2|/\sigma_1$ (using 1 to denote $0.6 < z < 1.0$ and 2 to denote $0.7 < z < 1.0$) for each mock realization. We find the quantity is greater than that of the DES Y1 data in 443 (29 per cent) of the mock realizations. Thus, the difference in α is not unusual.

At the end of Section 4, we found a correlation between the mean uncertainty and the scatter in α that suggested the obtained BAO likelihoods can generally be trusted. If these were to be true in all cases, it would suggest that we should use only the $0.7 < z < 1.0$ data for our DES Y1 measurement. To test this, we further consider the 8 per cent of mock realizations that exhibit more extreme behaviour in the ratio of uncertainties with and without removing the $0.6 < z < 0.7$ data. These realizations have been selected in order to have significantly greater uncertainty for the $0.6 < z < 1.0$ realizations and we indeed obtain $\langle\sigma_1\rangle = 0.073$ compared to $\langle\sigma_2\rangle = 0.054$. However, the standard deviations are flipped, $S_1 = 0.054$ compared to $S_2 = 0.061$. This suggests that in these cases, the uncertainty is significantly over-(under-) estimated for the $0.6 < z < 1.0$ ($0.7 < z < 1.0$) and that the underestimated $0.7 < z < 1.0$ uncertainty is actually a better match to the uncertainty of the $0.6 < z < 1.0$ results. In order to consider cases that are even more similar to our DES Y1 case, we take only the mocks out of this eight per cent that have an uncertainty less than 0.05 for $0.6 < z < 1$. This yields only 22 mocks. Their mean uncertainties are $\langle\sigma_1\rangle = 0.046$ and $\langle\sigma_2\rangle = 0.037$, to be compared to standard deviations of $S_1 = 0.047$ and $S_2 = 0.046$. While this is a limited number of mocks, the results are consistent with the conclusion that the uncertainty is underestimated in the cases where $0.7 < z < 1.0$ yields less uncertainty than the $0.6 < z < 1.0$ data.

The findings can be summarized as

(i) Eight per cent of the mock realizations are more extreme in terms of the comparison between the recovered $0.6 < z < 1.0$ and $0.7 < z < 1.0$ uncertainties.

(ii) These realizations have been chosen to have worse uncertainties for $0.6 < z < 1.0$; we find $\langle\sigma_\alpha\rangle = 0.073$ for $0.6 < z < 1.0$ and $\langle\sigma_\alpha\rangle = 0.054$ for $0.7 < z < 1.0$.

(iii) For these eight per cent of realizations, we find the standard deviations for the scatter in the recovered α values are 0.054 for $0.6 < z < 1.0$ and 0.061 for $0.7 < z < 1.0$.

(iv) Changing our criteria to be only cases where the $0.6 < z < 1.0$ uncertainty is less than 0.05 (and thus similar to our DES Y1 result) or simply $\sigma_2/\sigma_1 > 1$ (which is true for 30 per cent of the mock cases) yields consistent results.

Thus, for these cases, the uncertainties are generally underestimated for $0.7 < z < 1.0$ and we consider the $0.6 < z < 1.0$ result more trustworthy.

[1]*Cerro Tololo Inter-American Observatory, National Optical Astronomy Observatory, Casilla 603, La Serena, Chile*
[2]*Department of Physics and Astronomy, University College London, Gower Street, London WC1E 6BT, UK*
[3]*Department of Physics and Electronics, Rhodes University, PO Box 94, Grahamstown 6140, South Africa*
[4]*Institute of Space Sciences (ICE, CSIC) and Institut d'Estudis Espacials de Catalunya (IEEC), Campus UAB, Carrer de Can Magrans, s/n, E-08193 Barcelona, Spain*
[5]*Fermi National Accelerator Laboratory, PO Box 500, Batavia, IL 60510, USA*
[6]*Laboratório Interinstitucional de e-Astronomia - LIneA, Rua Gal. José Cristino 77, Rio de Janeiro, RJ - 20921-400, Brazil*
[7]*Instituto de Fisica Teorica, Universidade Estadual Paulista, Sao Paulo, Brazil*
[8]*Institute of Cosmology and Gravitation, University of Portsmouth, Portsmouth PO1 3FX, UK*
[9]*Instituto de Fisica Teorica UAM/CSIC, Universidad Autonoma de Madrid, E-28049 Madrid, Spain*
[10]*Institute of Astronomy, University of Cambridge, Madingley Road, Cambridge CB3 0HA, UK*
[11]*Kavli Institute for Cosmology, University of Cambridge, Madingley Road, Cambridge CB3 0HA, UK*
[12]*Department of Physics, University of Florida, Gainesville, FL 32611, USA*
[13]*GRAPPA, Institute of Theoretical Physics, University of Amsterdam, Science Park 904, 1090 GL, Amsterdam*
[14]*Lorentz Institute, Leiden University, Niels Bohrweg 2, Leiden, NL-2333 CA, The Netherlands*
[15]*LSST, 933 North Cherry Avenue, Tucson, AZ 85721, USA*
[16]*Observatories of the Carnegie Institution of Washington, 813 Santa Barbara St., Pasadena, CA 91101, USA*
[17]*Department of Physics and Astronomy, University of Pennsylvania, Philadelphia, PA 19104, USA*
[18]*CNRS, UMR 7095, Institut d'Astrophysique de Paris, F-75014, Paris, France*
[19]*Institut d'Astrophysique de Paris, Sorbonne Universités, UPMC Univ Paris 06, UMR 7095, F-75014, Paris, France*
[20]*SLAC National Accelerator Laboratory, Menlo Park, CA 94025, USA*
[21]*Kavli Institute for Particle Astrophysics and Cosmology, Stanford University, PO Box 2450, Stanford, CA 94305, USA*
[22]*Departamento de Física Matemática, Instituto de Física, Universidade de São Paulo, CP 66318, São Paulo, SP-05314-970, Brazil*

[23]*Observatório Nacional, Rua Gal. José Cristino 77, Rio de Janeiro, RJ - 20921-400, Brazil*
[24]*National Center for Supercomputing Applications, 1205 West Clark St., Urbana, IL 61801, USA*
[25]*Department of Astronomy, University of Illinois at Urbana-Champaign, 1002 W. Green Street, Urbana, IL 61801, USA*
[26]*Institut de Física d'Altes Energies (IFAE), The Barcelona Institute of Science and Technology, Campus UAB, E-08193 Bellaterra (Barcelona) Spain*
[27]*Kavli Institute for Cosmological Physics, University of Chicago, Chicago, IL 60637, USA*
[28]*School of Physics and Astronomy, Sun Yat-Sen University, Guangzhou 510275, China*
[29]*Centro de Investigaciones Energéticas, Medioambientales y Tecnológicas (CIEMAT), Madrid, Spain*
[30]*George P. and Cynthia Woods Mitchell Institute for Fundamental Physics and Astronomy, and Department of Physics and Astronomy, Texas A&M University, College Station, TX 77843, USA*
[31]*Department of Physics, IIT Hyderabad, Kandi, Telangana 502285, India*
[32]*Jet Propulsion Laboratory, California Institute of Technology, 4800 Oak Grove Dr., Pasadena, CA 91109, USA*
[33]*Department of Astronomy/Steward Observatory, 933 North Cherry Avenue, Tucson, AZ 85721-0065, USA*
[34]*Jodrell Bank Center for Astrophysics, School of Physics and Astronomy, University of Manchester, Oxford Road, Manchester M13 9PL, UK*
[35]*Department of Astronomy, University of Michigan, Ann Arbor, MI 48109, USA*
[36]*Department of Physics, University of Michigan, Ann Arbor, MI 48109, USA*
[37]*Fakultät für Physik, Universitäts-Sternwarte, Ludwig-Maximilians Universität München, Scheinerstr. 1, D-81679 München, Germany*
[38]*Department of Physics, ETH Zurich, Wolfgang-Pauli-Strasse 16, CH-8093 Zurich, Switzerland*
[39]*Santa Cruz Institute for Particle Physics, Santa Cruz, CA 95064, USA*
[40]*Department of Physics, The Ohio State University, Columbus, OH 43210, USA*
[41]*Center for Cosmology and Astro-Particle Physics, The Ohio State University, Columbus, OH 43210, USA*
[42]*Max Planck Institute for Extraterrestrial Physics, Giessenbachstrasse, D-85748 Garching, Germany*
[43]*Event Horizon Telescope, Harvard-Smithsonian Center for Astrophysics, MS-42, 60 Garden Street, Cambridge, MA 02138, USA*
[44]*Australian Astronomical Observatory, North Ryde, NSW 2113, Australia*
[45]*Argonne National Laboratory, 9700 South Cass Avenue, Lemont, IL 60439, USA*
[46]*Département de Physique Théorique and Center for Astroparticle Physics, Université de Genev´e, 24 quai Ernest Ansermet, CH-1211 Geneva, Switzerland*
[47]*Department of Astronomy, The Ohio State University, Columbus, OH 43210, USA*
[48]*Department of Astrophysical Sciences, Princeton University, Peyton Hall, Princeton, NJ 08544, USA*
[49]*Institució Catalana de Recerca i Estudis Avançats, E-08010 Barcelona, Spain*
[50]*Faculty of Physics, Ludwig-Maximilians-Universität, Scheinerstr. 1, D-81679 Munich, Germany*
[51]*Excellence Cluster Universe, Boltzmannstr. 2, D-85748 Garching, Germany*
[52]*Department of Physics and Astronomy, Pevensey Building, University of Sussex, Brighton BN1 9QH, UK*
[53]*ICTP South American Institute for Fundamental Research Instituto de Física Teórica, Universidade Estadual Paulista, São Paulo, Brazil*
[54]*Department of Physics, University of Arizona, Tucson, AZ 85721, USA*
[55]*Instituto de Física, UFRGS, Caixa Postal 15051, Porto Alegre, RS - 91501-970, Brazil*
[56]*Brookhaven National Laboratory, Bldg 510, Upton, NY 11973, USA*
[57]*School of Physics and Astronomy, University of Southampton, Southampton SO17 1BJ, UK*
[58]*Instituto de Física Gleb Wataghin, Universidade Estadual de Campinas, 13083-859 Campinas, SP, Brazil*
[59]*Computer Science and Mathematics Division, Oak Ridge National Laboratory, Oak Ridge, TN 37831, USA*
[60]*Department of Physics, Stanford University, 382 Via Pueblo Mall, Stanford, CA 94305, USA*

This paper has been typeset from a TEX/LATEX file prepared by the author.